

NO-A100 020

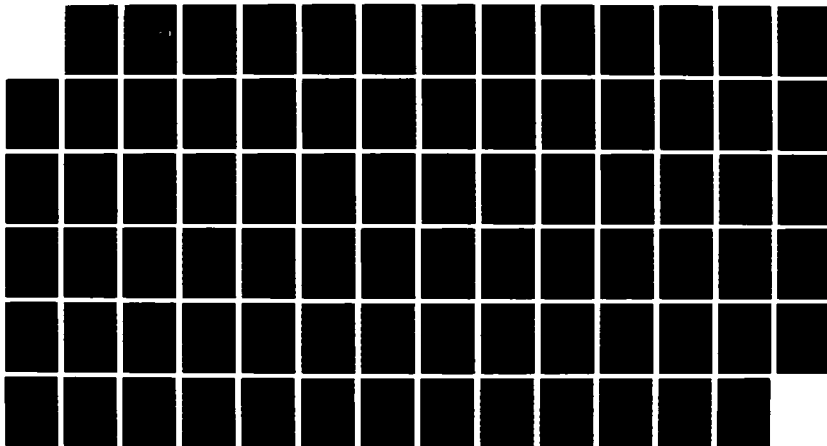
RADIAL MIXING IN TURBOMACHINES(U) VRIJE UNIV BRUSSELS
(BELGIUM) DEPT OF FLUID MECHANICS J DERUYCK ET AL.
15 APR 87 VUB-TN-39 AFOSR-TR-87-1423 AFOSR-85-0167

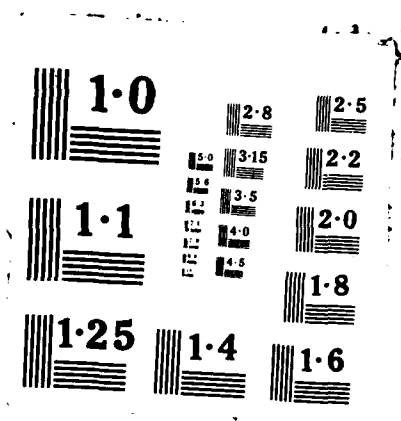
1/1

UNCLASSIFIED

F/O 20/4

NL





DTIC FILE COPY

AFOSR-TK. 87-1423

AD-A188 028

RADIAL MIXING IN TURBOMACHINES

Approved for public release;
distribution unlimited.

by

DE RUYCK J., HIRSCH Ch., TOORMAN E.

Dept. of Fluid Mechanics
Vrije Universiteit Brussel
Pleinlaan 2, 1050 Brussels
Belgium

DTIC
ELECTE
NOV 16 1987
S H D

April, 1987

Interim Scientific Report
September 1, 1985 - August 31, 1986
VUB-TN-39

Approved for public release; distribution unlimited.

- Prepared for -

Air Force Office for Scientific Research
Bolling AFB, USA
and
European Office for Aerospace Research and Development
London, England

AIR FORCE OFFICE OF SCIENTIFIC RESEARCH (AFSC)
NOTED FOR REVIEW - TAL TO DTIC
1. This report was reviewed and approved and is
being distributed to the AFSC (AFR 190-12).
2. This report is being distributed to the AFSC
Chaf. Technical Information Division

UNCLASSIFIED

SECURITY CLASSIFICATION OF THIS PAGE

REPORT DOCUMENTATION PAGE

1a. REPORT SECURITY CLASSIFICATION Unclassified			1b. RESTRICTIVE MARKINGS		
2a. SECURITY CLASSIFICATION AUTHORITY			3. DISTRIBUTION/AVAILABILITY OF REPORT Approved for public release Distribution unlimited		
2b. DECLASSIFICATION/DOWNGRADING SCHEDULE					
4. PERFORMING ORGANIZATION REPORT NUMBER(S) VUB-TN-39			5. MONITORING ORGANIZATION REPORT NUMBER(S) AFOSR-TR- 87-1423		
6a. NAME OF PERFORMING ORGANIZATION Vrije Universiteit Brussel Dept. of Fluid Mechanics		6b. OFFICE SYMBOL (If applicable) VUB-STRO	7a. NAME OF MONITORING ORGANIZATION European office for Aerospace Research and Development		
6c. ADDRESS (City, State and ZIP Code) Pleinlaan 2 1050 BRUSSELS BELGIUM			7b. ADDRESS (City, State and ZIP Code) Marylebone Road LONDON ENGLAND		
8a. NAME OF FUNDING/SPONSORING ORGANIZATION Air Force Office for Scientific Research		8b. OFFICE SYMBOL (If applicable) AFOSR/NA	9. PROCUREMENT INSTRUMENT IDENTIFICATION NUMBER AFOSR-85-0167		
8c. ADDRESS (City, State and ZIP Code) Building 410 Bolling AFBDC 20332-6448 USA			10. SOURCE OF FUNDING NOS.		
			PROGRAM ELEMENT NO.	PROJECT NO.	TASK NO.
11. TITLE (Include Security Classification) Radial mixing in Turbomachines			61102F 2307 SI		
12. PERSONAL AUTHOR(S) De Ruyck J. Hirsch Ch. Toorman E.					
13a. TYPE OF REPORT annual		13b. TIME COVERED FROM 85-9-1 TO 86-8-31		14. DATE OF REPORT (Yr., Mo., Day) 87-4-15	
15. PAGE COUNT 79					
16. SUPPLEMENTARY NOTATION					
17. COSATI CODES			18. SUBJECT TERMS (Continue on reverse if necessary and identify by block number)		
FIELD	GROUP	SUB. GR.	Radial Mixing		
			Secondary flow		
			Wakes		
19. ABSTRACT (Continue on reverse if necessary and identify by block number)					
<p>The main tools for the prediction of convective radial mixing are developed.</p> <p>The secondary flows needed for the convective mixing are found from pitch averaged vorticity equations combined with integral methods for the computation of 3D end-wall boundary layers, 3D profile boundary layers and 3D asymmetric wakes. This integral approach requires less approximations than previous radial mixing theories and only three empirical constants are required. The convective mixing coefficient of Adkins and Smith is found from the resulting secondary flow velocities.</p> <p>The method is applied to some standard test cases, where secondary flow patterns are compared with available test data.</p>					
20. DISTRIBUTION/AVAILABILITY OF ABSTRACT UNCLASSIFIED/UNLIMITED <input checked="" type="checkbox"/> SAME AS RPT. <input checked="" type="checkbox"/> DTIC USERS <input type="checkbox"/>			21. ABSTRACT SECURITY CLASSIFICATION Unclassified		
22a. NAME OF RESPONSIBLE INDIVIDUAL DR JAMES WILSON			22b. TELEPHONE NUMBER (Include Area Code) 212-767-4935		22c. OFFICE SYMBOL AFOSR/NA

DTIC
COPY
INSPECTED

Codes

Dist. and/or
Special

DD FORM 1473, 83 APR

87 10 14 388

EDITION OF 1 JAN 73 IS OBSOLETE.

Unclassified
SECURITY CLASSIFICATION OF THIS PAGE

CONTENTS

Contents	2
Nomenclature	3
 Chapter 1 : Introduction	 5
 Chapter 2 : Historical background	 6
2.1 Passage vortex	6
2.2 Trailing edge vorticity	7
2.3 Tip clearance flows	8
2.4 Profile boundary layer radial flows	8
2.5 Wake radial flows	8
2.6 Radial diffusion	8
2.7 Two approached for secondary flows	9
2.8 Radial mixing process	10
2.9 Experimental work	10
 Chapter 3 : Approach	 11
3.1 Through flow computation	12
3.2 End-wall boundary layer computation	13
3.3 Passage radial flow computation	14
3.4 Blade profile boundary layers and wakes	15
 Chapter 4 : End-wall boundary layer computations	 16
 Chapter 5 : Main passage inviscid secondary flows	 20
5.1 Secondary flow momentum equation	20
5.2 Superposition of secondary flows	23
5.3 Secondary flow continuity equation	23
5.4 Practical solution procedure	24
 Chapter 6 : Blade profile boundary layers	 26
6.1 Momentum equations in meridional coordinates	26
6.2 Entrainment and skin friction	28
6.3 Profile models	31
6.4 Practical solution procedure	33
 Chapter 7 : Wake analysis	 34
7.1 Wake profiles	34
7.2 Integral wake momentum equations	36
7.3 Local wake decay equation	37
7.4 Practical solution procedure	40
 Chapter 8 : Trailing edge and near wake	 42
 Chapter 9 : Results	 44
9.1 Isolated airfoil	44
9.2 Onera rotor	44

9.3 Dring rotor	45
Conclusions	47
Future work	48
References	49
Figures	52
Appendix A : Some notions of curvature	60
Appendix B : Momentum equations in curvilinear coordinates ...	64
Appendix C : Integral boundary layer parameters	71
Appendix D : Integral wake parameters	76

NOMENCLATURE

b	boundary layer parameter
C_f	friction coefficient
c	absolute velocity component, chord
E	entrainment rate
F	force defect thickness
f	blade force, wake model (eq (7.4))
g	wake model (eq (7.7))
H	shape factor
H^*	Head's shape factor
h	annulus height, metric coefficient
m	meridional coordinate
n	coordinate normal to the end-walls
p	static pressure
R_{ij}	radii of curvature (appendix A)
r	radius, recovery factor
s	streamwise coordinate, pitch
T	temperature
T_t	total temperature
T_r	recovery temperature
T^*	Eckert reference temperature
t	transverse coordinate
t_c	tip clearance
U	wheel speed
u	pitchwise coordinate
W	velocity in the blade reference system
w	relative velocity component

x orthogonal coordinate
 α radial flow angle
 β passage flow angle
 γ stagger angle
 δ physical boundary layer thickness
 δ^* displacement thickness
 ϵ skewing angle, diffusion coefficient
 ϵ_w wall skewing angle
 η u/δ
 θ momentum thickness, angular coordinate
 λ correction momentum thickness
 ν viscosity, eddy viscosity
 ρ density
 σ solidity, wall inclination angle (fig 3.1)
 τ shear stress
 ω vorticity vector

Subscripts

k kinematic
 w at the wall
 m, n, u in meridional coordinates (fig. 3.1)
 s, n, t in streamline coordinates (fig. 6.1)
 sec secondary flow
 $ewbl$ end-wall boundary layer
 inv inviscid

Superscripts

\wedge inviscid flow parameter
 \sim passage-averaged value
 $'$ expressed in s, t coordinates (figure 6.1)

Abbreviations

EWBL end-wall boundary layer
 PBL profile boundary layer
 3D three-dimensional

1. INTRODUCTION

The main objective of the present research is to provide a method for the prediction of detailed flow properties in a multistage axial compressor, in particular the secondary flow patterns and the radial mixing process.

The background of the present work lies in a Quasi 3D approach [1]. In this approach, correlations are used to compute the passage-averaged profile losses and deviations. End-wall boundary layers (EWBL) are predicted through an 3D integral method where end-wall secondary flows and clearance effects are introduced [2,3].

In this EWBL approach, it is assumed that all the secondary and tip clearance effects originate inside the EWBL and extra losses are taken into account separately when computing the machine efficiency [3]. However, the interaction between the secondary flows and the main compressor flow is stronger than a simple efficiency correction [4,5,6,7,8]. The present trend towards higher stage loadings and lower aspect ratio's enhances the effect of radial redistributions but current axisymmetric calculation methods are not able to account for it. This interaction is illustrated on figure 1.1 where a radial distribution of temperature is shown with and without radial redistribution effects.

In the present project, a technique for the determination of the radial mixing is being developed. This technique is based on the determination of the radial flow components as obtained from integral boundary layer and wake predictions.

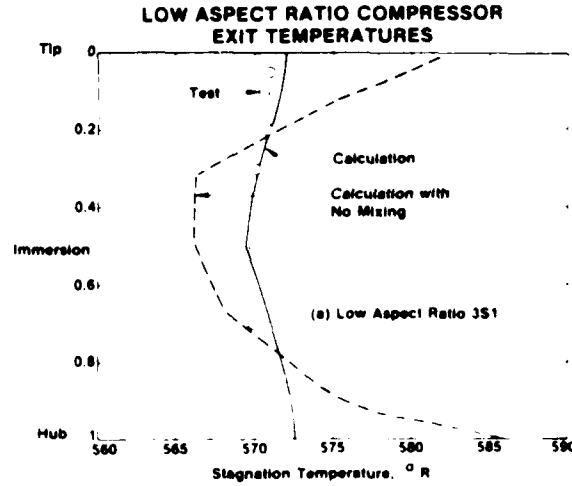


Figure 1.1 : Radial redistribution of total temperature [8]

Adkins & Smith [8] presented a basic formulation for the determination of radial mixing effects. In their approach, a large number of parameters determining the secondary flow are to be chosen on an empirical basis. In the present approach, the velocity profile families built in the integral boundary layers and wakes lead to a prediction of most of these parameters and it allows the reconstruction of the secondary flow pattern, with much less additional parameters.

As shown by Adkins and Smith [8], the radial mixing can be expressed through a diffusion type equation where the 'diffusion' or 'mixing'

coefficient is a function of the rms radial velocity. When the radial velocity is well known this mixing coefficient can be easily estimated. Gallimore and Cumpsty [6] showed that mixing due to turbulent diffusion may be as important as mixing due to radial convection and an additional turbulent mixing coefficient is to be considered. When the total mixing coefficient is known, the mixing equation can easily be solved using a finite difference or finite element method with Neumann type boundary conditions.

2. HISTORICAL BACKGROUND

During the last twenty years, the design requirements for axial compressors have increased considerably calling for more advanced computational methods. However, because of the high complexity of the flow pattern, no complete three-dimensional calculation methods can presently be developed which would account for multistage configurations. The flow is to be computed by parts which interact with each other.

The current approach consists in the splitting of the turbomachine flow into two two-dimensional flows [1]. The first flow is considered in a circumferential blade-to-blade surface (S1) and the second is the circumferentially averaged meridional flow (S2). Different secondary effects which are not considered in these S1 and S2 flows are to be computed separately and superposed in an interactive way. The different secondary flows are summarised on figure 2.1. These flows occur in a surface normal to S1 and S2, which is not considered in the basic Quasi 3D approach.

In the following, the different contributions shown on figure 2.1 will be reviewed separately (sections 2.1 to 2.6). Two different approaches for the determination of the secondary flows are reviewed in section 2.7. Section 2.8 discusses radial mixing processes and section 2.9 is a brief review of experimental work in this field.

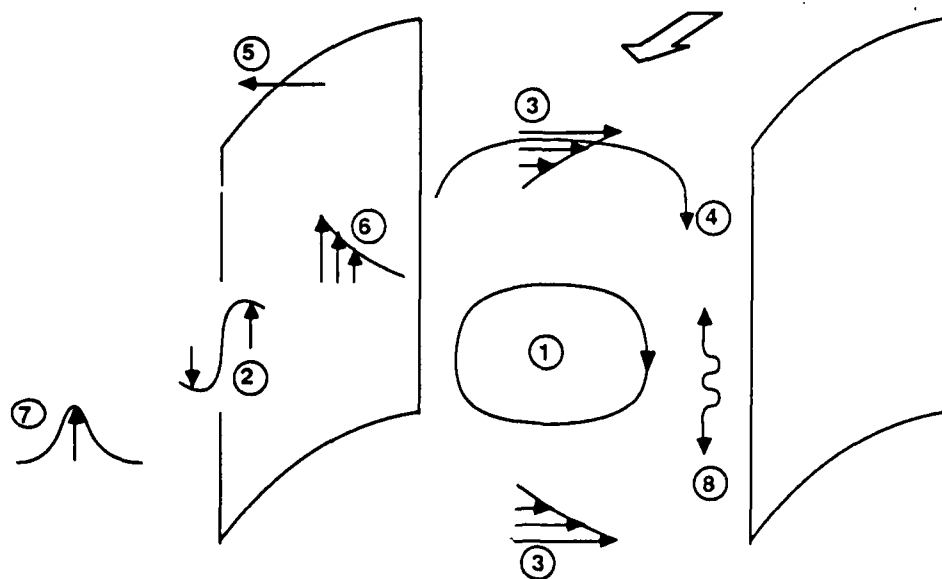
2.1 Passage vortex (contributions 1,3,4)

The passage vortex is a well known secondary flow component in turbomachine flows. Its mechanism has been investigated a first time by Carter and Cohen for uniform flows with thin boundary layers [26] and by Squire and Winter for nonuniform flows [27]. It was further investigated by Hawthorne [12] and A.G. Smith [13] for cascades and by Dixon [14] for rotating blade rows.

The passage vortex is basically a streamwise vorticity component caused by the deflection of a non-uniform mainstream velocity. It can be obtained from the conservation of momentum in a steady, inviscid incompressible fluid [26,27]

$$\vec{\nabla} \wedge (\vec{W} \wedge \vec{\omega}) = 0 \quad (2.1)$$

The inviscid equation (2.1) is often applied over the whole passage, including the viscous boundary layers. In a different approach (see 2.7), the flow is considered as a superposition of (i) a main inviscid primary flow, and (ii) viscous boundary layer flows which are treated through



- Flow :
- 1 Main passage vortex
 - 2 Trailing shed and filament vortex
 - 3 End wall boundary cross flow
 - 4 End wall boundary layer passage vortex
 - 5 Tip clearance flow
 - 6 Profile boundary layer radial flow
 - 7 Wake radial flow
 - 8 Radial diffusion

- Origin :
- Flow non-uniformities
 - Spanwise changes in circulation
 - Boundary layer overturning
 - Boundary layer overturning
 - Tip clearance pressure difference
 - Centrifugation
 - Centrifugation
 - Turbulence

Figure 2.1 : Secondary flows

integral boundary layer methods. In the latter case, a distinction is to be made between a 'main passage vortex' caused by an overall non-uniform inlet flow as predicted by a through-flow computation, and an 'end-wall boundary layer passage vortex'.

2.2 Trailing edge vorticity (contribution 2)

The vortex sheet leaving the trailing edge of the blade has two components : the trailing filament and the trailing shed vorticities. The shed vorticity is due to the changes in circulation along the span, the filament vorticity is due to the stretching of vortex filaments and is a result of non-uniformities in the inlet flow. Circulation changes can be due either to an overall non-free vortex behaviour of the passage flow, either to specific changes in blade loading inside the end-wall boundary layers.

These components were investigated a first time by Hawthorne [28] and Came and Marsh [29] on the basis of inviscid flow models.

2.3 Tip clearance flows (contribution 5)

Tip clearance flows contribute to the secondary flow motion in an important way. They affect the passage vortex by modifying the flow turning and the trailing edge vortex through a change in blade loading. Smith [11] proposed an inviscid approach where tip clearance and leakage secondary flows are taken into account. Several empirical constants were introduced. In an approach where boundary layer flows are considered separately, tip clearance effects can be included in the integral boundary layer equations [3] (see 2.7).

2.4 Profile boundary layer radial flows (contribution 6)

Boundary layers along turbomachine blades are three dimensional and contribute to the radial convection. Both experimental and theoretical information about these radial flows is poor. Adkins and Smith [8] estimated these radial flows by solving the local conservation of radial momentum along the blade, introducing two empirical constants. The radial velocity was found to be a direct consequence of the boundary layer velocity gradient. Their development is inviscid, in the same way as was done for the passage vortex. Whitfield and Keith [30] used the same base but included the blade loading effects by means of the loss correlations of Koch and Smith.

Viscous 3D boundary layer applications on turbomachine blades are almost inexistant. More experimental information has recently been made available by Lakshminarayana and Popovski [24].

2.5 Wake radial flows (contribution 7)

The wake can be considered as an important element in the total radial flow analysis. Peak values in radial velocity are observed in the near wake, where very low velocities may induce a high centrifugation. Adkins and Smith [8] and Whitfield and Keith [30] treated the wake by writing the mainstream and radial momentum conservation laws along the wake center. The total amount of radial flow is found by modeling the wake profiles. Since symmetric wake models are used, there is no ability to simulate asymmetric radial wake profiles. Hah and Lakshminarayana [31] made full turbulent 3D computations in asymmetric wakes with radial flows. These computations are in good agreement with detailed experiments, but their cost may be in disproportion to the gain in useful information.

2.6 Radial diffusion (contribution 8)

All the above radial flows contribute to radial mixing by a convection mechanism. Gallimore and Cumpsty [6,7] showed that at least in their test compressor the radial energy redistribution is due mainly to turbulent diffusion. They based their conclusion on the facts (i) that the observed mixing was isotropic [6] and (ii) that the measured turbulent energy production is almost fully compensated by turbulent energy diffusion, which means that convection phenomena are of less importance [7].

2.7 Two approaches for secondary flows

From the the above discussion on secondary flows, it follows that a part of them originate in three viscous layers :

- (i) the end-wall boundary layers
- (ii) the profile boundary layers
- (iii) the wakes

The cross flows in these layers may be estimated in two ways :

- (i) solving local inviscid equations over the whole span, including the viscous layers
- (ii) exclude the viscous layers from the inviscid solution and solving them separately by means of integral boundary layer and wake equations

The first approach has been referred to in sections 2.1 to 2.4 [8,11,12,13,14,26,27,28,29,30,31]. A large amount of such inviscid secondary flow approaches is reviewed in the AGARD conference proceedings 214 (1977) about 'Secondary Flows in Turbomachines' [25].

In the integral boundary layer and wake approach, secondary flows are predicted in a less detailed way, whereas viscous effects can be taken into account. Secondary flows are characterised by some integral cross flow thicknesses which quantify a total amount of secondary mass and momentum flow.

Early 3D end-wall boundary layer (EWBL) equations were proposed by Cooke and Hall [15] and Horlock [16]. Smith [17] showed the presence of variations in blade loading inside the boundary layers, which can affect the secondary flow in an important way, and he showed the importance of the tip clearance effects. Mellor & Wood [9] and Horlock & Perkins [18] took these effects into account through the introduction of force defects. De Ruyck & Hirsch [3] extended this theory by introducing (i) new correlations for the force defects and (ii) profile model equations suited for turbomachine EWBL flows, which allow the reconstruction of complete spanwise pitch averaged cross flow profiles. Only two empirical constants which are extensively calibrated are present in this method.

Detailed 3D profile boundary layer (PBL) and wake equations are less profuse and as a first step in the present project, 3D boundary layer and wake equations were developed in fully curvilinear coordinates. This development is applied in a coherent way for EWBL as well as PBL and wakes. Recent theoretical developments of full 3D boundary layer equations are summarised in [25]. This reference discusses the problem of separations, a problem which is not yet treated in the present report, but which is to be included in the future since it appears from the available test cases that the trailing edge separation plays an important role in the near wake, including the induction of radial flows.

Although inviscid theories are important for the understanding of secondary flows, these theories are practically not applied in multistage design codes, except for radial flows along profiles and in wakes. The present proposal therefore seeks for a complete integral approach for the secondary flow description. Integral secondary flow results are next used as input for the description of the radial mixing process.

2.8 Radial mixing process [8]

Adkins & Smith [8] proposed a diffusion type mixing equation which can be applied for the mixing of any flow parameter. The 'diffusion' or 'mixing' coefficient is determined from the knowledge of the secondary flow, which in their case is obtained from Smith's inviscid secondary flow approach. Some applications in [8] show the importance and the correct behaviour of this mixing theory. More recently, Gallimore and Cumpsty [7] presented much simpler computations based on the turbulent mixing only. Whitfield and Keith [30] made a more clear distinction between convection and diffusion mechanisms. They did not consider the convection as being isotropic, as was done by Adkins through the use of a diffusion type equation. They rather traced the flow particles and obtained non-isotropic flow property migrations in the spanwise direction.

The three above approaches are validated by experiments, although the mechanisms they use are very different. This validation is however obtained through the calibration of empirical constants, which probably compensates the shortcomings of these approaches. In order to clarify this situation, one of the scopes of the present work will be to determine the relative importance of mixing through convection and mixing through turbulent diffusion. The diffusion type equation of Adkins & Smith will be applied in the present approach and any flow property ϕ will be radially redistributed through

$$\frac{\partial \phi}{\partial m} = \epsilon \frac{\partial^2 \phi}{\partial n^2} \quad (2.1)$$

where, combining convection and diffusion,

$$\epsilon \approx \int_{\text{pitch}} \frac{w_n^2}{w_m^2} d\theta + \text{turbulent diffusion coefficient} \quad (2.2)$$

w_m and w_n denote the meridional and radial velocities, θ the angular coordinate. Equation (2.1) does not include mixing losses, it only expresses the mixing process. It can easily be solved through a numerical scheme. The energy conservation is obtained through a Neumann-type boundary condition which expresses that there is no enthalpy or entropy flux through the end-walls. Mixing losses can eventually be added through source terms in equation 2.1.

2.9 Experimental work

Besides theoretical developments, experimental data can be found. A classical test case is the Languier Rotor [5] tested at ONERA. Test data are available downstream of a rotor blade row, showing a radial flow profile which can be interpreted as a superposition of the different secondary flow contributions [8]. Dring et al [4] made extensive experiments at four stations downstream of a rotor blade row, at several radial positions, and at four different flow rates. Other wake data are available from the Pennsylvania State University [32,33]. Two three-stage compressors, differing primarily in aspect ratio, were designed and tested at Pratt & Whitney Aircraft under NASA sponsorship [34,35]. The effects of mixing are seen to be very strong for both configurations (see figure 1.1).

Less detailed data are available for the profile boundary layer radial flows. Recently, data were made available by Lakshminarayana and Popovski [24]. Extensive data are presented at both pressure and suction side of a compressor rotor blade, at five radial positions and three axial stations.

3. APPROACH

In the following sections it will be discussed in which way the different radial flows (figure 2.1) will be investigated. There is an essential difference with the Adkins and Smith [8] and Whitfield and Keith [30] approaches through the use of integral methods, reducing the amount of empirical constants. The approach which will be used for the radial mixing process will be based on equations (2.1) and (2.2). The present report is limited to the radial flow prediction.

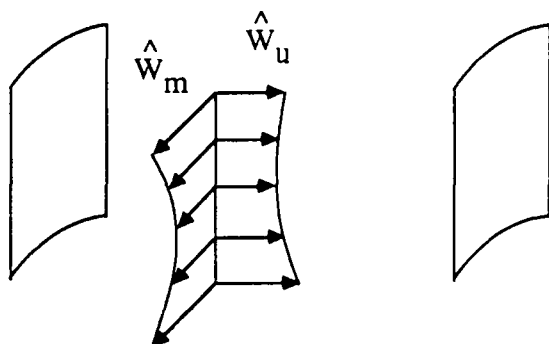
The strategy which is used is illustrated on figure 3.1. Four steps can be considered in the global flow computation :

- (i) Through flow computation
- (ii) Computation of end-wall boundary layers
- (iii) Computation of the passage radial flows
- (iv) Computation of profile boundary layers and wakes

All the equations are expressed in a meridional coordinate system m, n, u which is shown on figure 3.2. The secondary flows are determined in a surface normal to the $S1$ and $S2$ surfaces, that is surfaces of constant meridional coordinate m .

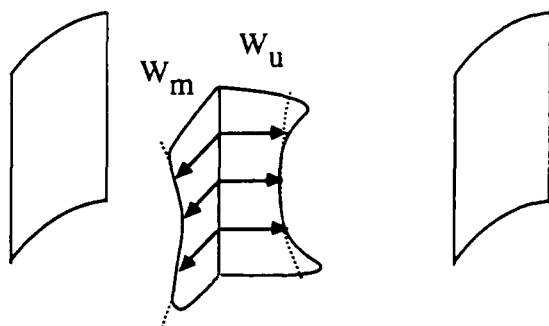
3.1 Through flow computation

The computation of the radial effects needs input from the main flow computations, or eventually from experiment. In practice a Quasi 3D computation is performed which yields the spanwise passage averaged profiles of all the flow properties. Amongst these are the meridional and angular velocity components \hat{w}_m and \hat{w}_u , and the unmixed temperature profiles. The velocity profiles are input for the next step in the calculation procedure.



THROUGH FLOW COMPUTATION :

passage averaged velocities

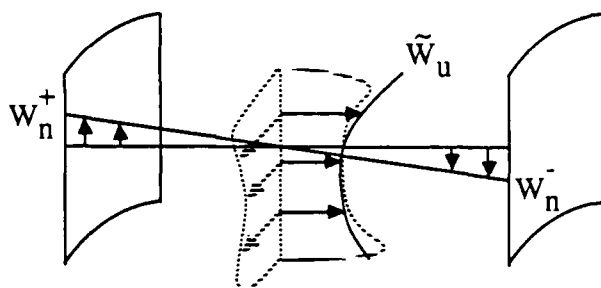


END-WALL BOUNDARY LAYER COMPUTATION :

passage averaged velocities including :

- EWBL viscous effects
- EWBL cross flows
- Tip clearance flows

see equations (3.1) and (3.2)

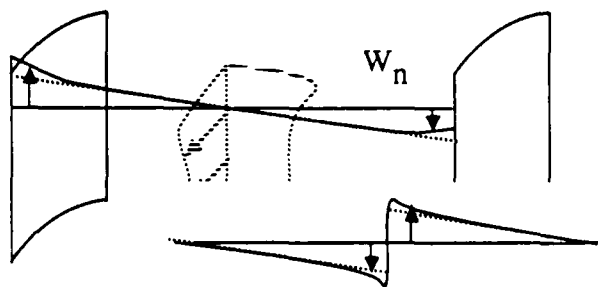


PASSAGE RADIAL FLOW COMPUTATION :

Passage radial flows including :

- All EWBL effects
- Main flow non-uniformity effects
- Circulation changes

see equation (3.8)



PROFILE BOUNDARY LAYER AND WAKE COMPUTATION :

Detailed radial velocities including
profile boundary layer and wake radial flows

Figure 3.1 : Strategy for the radial flow computation

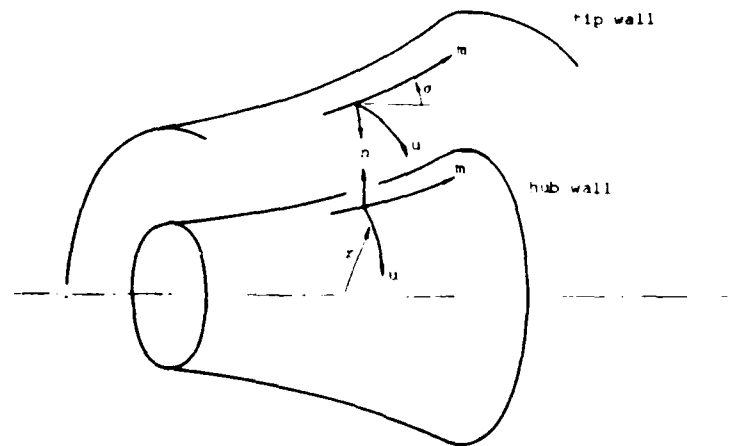


figure 3.2 : meridional coordinate system

3.2 End-wall boundary layer computation

The EWBL calculation method as presented in [3] can directly be used. In this method passage averaged EWBL equations are fully developed in the curvilinear meridional coordinate system, including all curvature, Coriolis and centrifugal effects. Appropriate EWBL velocity profiles, developed for the particular case of a turbomachine, are used.

The inclusion of the boundary layer equations yield passage averaged velocity profiles w_m and w_u where

$$w_m = \hat{w}_m - w_{m.ewbl} \quad (3.1)$$

$$w_u = \hat{w}_u - w_{u.ewbl} \quad (3.2)$$

$w_{m.ewbl}$ and $w_{u.ewbl}$ are the velocity defects present in the boundary layers. According to [3], the resulting passage averaged secondary flow in the surface $m=cte$ is given by

$$\begin{aligned} \tilde{w}_{u.sec.ewbl} &= w_u - w_m \hat{tg\beta} \\ \text{where } \hat{tg\beta} &= \frac{\hat{w}_u}{\hat{w}_m} \end{aligned} \quad (3.3)$$

This secondary velocity is zero in case of a collateral EWBL flow ($\beta = \hat{\beta}$) It implicitly takes into account the effects of :

- viscosity
- tip clearance
- passage and trailing edge vorticities caused by EWBL velocity defects.

The EWBL calculation procedure is summarized in section 4.

3.3 Passage radial flow computation

The radial flows inside the passage are found from the incompressible inviscid vorticity equation

$$(\vec{W} \cdot \vec{\nabla}) \cdot \vec{\omega} - (\vec{\omega} \cdot \vec{\nabla}) \cdot \vec{W} = 0 \quad (3.4)$$

Since the secondary flow is searched in surfaces $m = \text{cte}$, only the meridional component of the secondary vorticity is relevant

$$\omega_m = \frac{1}{r} \frac{\partial r w_u}{\partial n} - \frac{1}{r} \frac{\partial w_n}{\partial \theta} = 0 \quad (3.5)$$

From the previous steps, some information is available about the passage average of the velocity w_u , whereas w_n is the searched velocity component.

The idea of the present approach is to passage average equations (3.4) and (3.5). This yields following equations (section 5)

$$\frac{\partial \bar{\omega}_m}{\partial m} = F \left(\bar{\omega}_m, [w_n]_+^-, \bar{w}_u, \frac{\partial \hat{w}_m}{\partial n} \right) \quad (3.6)$$

where

$$\bar{\omega}_m = \frac{1}{r} \frac{\partial}{\partial n} r \bar{w}_u - \frac{1}{s} [w_n]_+^- \quad (3.7)$$

The passage averaged velocity \bar{w}_u can be decomposed as

$$\bar{w}_u = \hat{w}_u + \bar{w}_{u.\text{sec.ewbl}} + \bar{w}_{u.\text{sec.inv}} \quad (3.8)$$

$[w_n]_+^-$ is the difference in radial velocity between pressure and suction side of the passage (see figure 3.1). Equation (3.8) superposes the velocities from the through flow computation (section 3.1), the EWBL flow (section 3.2)

and main passage secondary flow.

Equations (3.6) to (3.8) contain four unknowns : $\bar{\omega}_m$, $[\bar{w}_n]_+$, \bar{w}_u and $\bar{w}_{u.sec.inv}$. The continuity in the secondary flow surface is used as fourth equation to obtain closure. Some pitchwise modeling of the secondary flow velocities is required at this point, since pitchwise information is lost through the passage averaging. A linear behaviour for w_n and a quadratic behaviour for w_u yields [9]

$$\frac{\partial}{\partial n} [\bar{w}_n]_+ = \frac{8}{s} \bar{w}_{u.sec} \quad (3.9)$$

From equations (3.6) to (3.9), it is possible to reconstruct the radial velocities including

- all EWBL effects through $\bar{w}_{u.sec.ewbl}$
- main passage effects through $\partial_n \bar{w}_m$
- main circulation changes through $\partial_n r \bar{w}_u$

The only assumptions made consist in some pitchwise modelling of the secondary flow velocities, which results in an approximation in equation (3.9).

3.4 Blade profile boundary layers and wakes

These flows originate mainly from the centrifugation and coriolis effects in blade profiles and blade wakes. The corresponding 3D boundary layer equations automatically include these effects. In the present wake approach, pressure and suction side of the wake are treated separately and the concept of 'peak velocities' is not used. The reason for this is that wake profile may be very asymmetric. Pressure and suction side radial flows may even have opposite signs (Dring data [4]). An asymmetric 3D wake model equation is introduced.

When this last step is performed, radial flows are reconstructed anywhere in the passage flow and the radial mixing process through radial convection can be started.

4. END-WALL BOUNDARY LAYER COMPUTATIONS

The used method originates from Mellor and Wood's approach [9] where rigorous integral boundary layer equations were written for the end-wall boundary layers, including force defect thicknesses. In this work, simplified assumptions such as constant shape factor or skin friction were made and the equations were integrated from inlet to outlet of a blade row. This approach was extended by De Ruyck & Hirsch [3] to include velocity profile models and correlations for secondary flow and tip clearance effects through the so called defect forces.

The End-wall boundary theory presently used has been presented extensively in [2] and is briefly summarized below.

The basic equations are written in the meridional coordinate system m, n, u (fig 3.2). 'c' denotes an absolute velocity and 'w' a relative velocity component.

The boundary layer momentum and entrainment equations are

$$\frac{d}{dm} \rho c_m^2 \theta_{mm} + \rho c_m \delta_m^* \frac{dc_m}{dm} \quad (4.1)$$

$$- \rho c_m^2 \sin \sigma (\delta_u^* \tan \alpha + \theta_{uu}) = r \tau_m + r F_m$$

$$\frac{d}{dm} \rho c_m^2 \theta_{um} + \rho c_m \delta_m^* \frac{dc_u}{dm} \quad (4.2)$$

$$+ \rho c_m^2 \sin \sigma (\delta_m^* \tan \alpha + \theta_{um}) = r \tau_u + r F_u$$

$$\frac{1}{r \rho c_m} \frac{d}{dm} r \rho c_m (\delta - \delta_m^*) = \frac{E(H_k^*)}{\cos \alpha} \quad (4.3)$$

Eqs (4.1) to (4.3) are written in the absolute reference system. The boundary layer thicknesses in these equations are defined as

$$\theta_{ij} = \int_0^\delta \left(\frac{w_i}{w_m} - \frac{w_i}{w_m} \right) \frac{\rho w_j}{\rho w_m} dn \quad (4.4)$$

$$\delta_i^* = \int_0^{\delta} \left(\frac{\hat{\rho} \hat{w}_i}{\rho w_m} - \frac{\rho w_i}{\rho w_m} \right) dn \quad (4.5)$$

These thicknesses are defined in the wall reference system. The velocities with an overhead carat ($\hat{}$) denote the 'outer' or 'inviscid' reference velocities. Corrections for variations of these 'inviscid' values with the distance from the wall are not considered [2]. The velocity ratios are modelled through (figure 4.1)

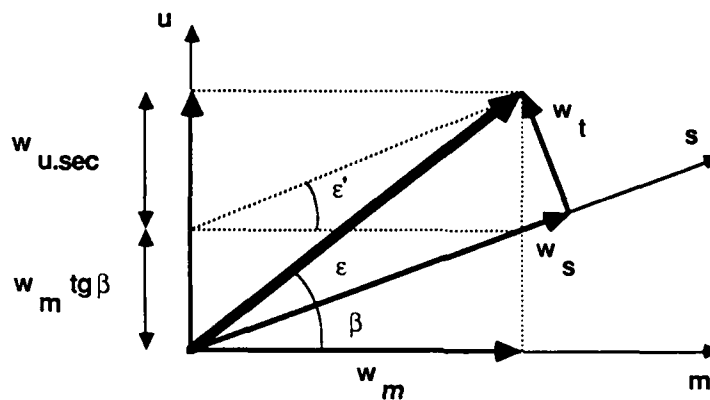


Figure 4.1 : velocity components

$$\frac{w_m}{\hat{w}_m} = 1 - b \left(1 - \frac{n}{\delta} \right)^n \quad (4.6)$$

$$\frac{w_{u.sec.ewbl}}{\hat{w}_m} = \frac{w_u - w_m \operatorname{tg} \alpha}{\hat{w}_m} = (1-b) \operatorname{tg} \epsilon'_w \left(1 - \frac{n}{\delta} \right)^n \quad (4.7)$$

where

$$b = \exp(-10n C_f^{.5} \cos \beta^{-.134}) \quad (4.8)$$

$$\operatorname{tg} \epsilon'_w = \operatorname{tg}(\epsilon_w + \beta) - \operatorname{tg} \beta \quad (4.9)$$

The density ratio is given by

$$\frac{\rho}{\rho} = 1 - 2a(1 - \frac{w_m}{x_m}) + a(1+4a)(1 - \frac{w_m}{x_m})^2 \quad (4.10)$$

$$a = .89 \frac{\gamma-1}{2} M_e^2 \quad (4.11)$$

The entrainment rate E is given by

$$E(H_k^*) = 0.0306 (H_k^* - 3.)^{0.653} \quad (4.12)$$

$$H_k^* = \frac{\delta - \delta_{mk}^*}{\theta_{mmk}} \quad (4.13)$$

The mainstream and cross flow shear stresses are obtained from

$$\tau_s = C_f \frac{\rho w_s^2}{2} \quad (4.14)$$

$$\tau_t = \tau_s t g \epsilon_w \quad (4.15)$$

where

$$C_f = 0.246 Re_{\theta_{mm}}^{-0.268} \left(\frac{T}{T^*} \right) \exp(-1.56 H_k) \quad (4.16)$$

$$H_k = \frac{\delta_{mk}^*}{\theta_{mmk}} \quad (4.17)$$

$$\frac{T}{T^*} = 1 + 0.72 a$$

The 'kinematic' thicknesses δ_{mk}^* and θ_{mmk} are defined as

$$\delta_{mk}^* = \int_0^\delta (1 - \frac{w_m}{x_m}) dn \quad (4.18)$$

$$\theta_{mmk} = \int_0^\delta (1 - \frac{w_m}{x_m}) \frac{w_m}{x_m} dn \quad (4.19)$$

Eqs (4.4) to (4.19) are written in the wall reference system. The thicknesses θ_{mm} , θ_{um} , δ^* and δ_u^* and the parameters b and n have the same

values in both absolute and relative systems whereas the wall skewing angles and θ_{uu} are related by the jump relations

$$(\text{tg}\epsilon'_w)^{\text{abs}} = (\text{tg}\epsilon'_w)^{\text{rel}} + \frac{1}{1-b} (\text{tg}\beta^{\text{rel}} - \text{tg}\beta^{\text{abs}}) \quad (4.20)$$

$$\theta_{uu}^{\text{abs}} = \theta_{uu}^{\text{rel}} + \gamma \delta_u^* / c_m$$

The blade mainstream defect force is found from

$$\frac{F_s}{\rho} = L \frac{w_s^2}{2\cos\gamma} \sigma C_L^2 \quad L = .01 \quad (4.21)$$

The tranverse lift defect is found from

$$\frac{F_t}{\rho} = - \frac{k}{s} w_s^2 \theta_{tm} \quad (4.23)$$

in absence of a tip clearance and from

$$\frac{F_t}{\rho} = \frac{t_c}{\cos\alpha} w_m \frac{dw_u}{dm} - \frac{k'}{s} w_s^2 \theta_{tm} \quad (4.24)$$

in presence of a tip clearance. The constants k and k' are given by

$$k \approx 3. \quad k' \approx .5 \quad (4.25)$$

The cross flow thickness is defined through

$$\theta_{tm} = - \cos\alpha \int_0^\delta \frac{w_t}{w_s} \frac{w_m}{w_s} dn \quad (4.26)$$

$$\theta_{tm} = (\theta_{um} - \theta_{mm} \text{tg}\beta) \cos^2\beta$$

Eqs (4.21) to (4.26) are written in the blade reference system.

The basic eqs (4.1), (4.2) and (4.3) are integrated in the meridional direction using a fifth order Runge-Kutta method with as complementary relations eqs (4.4) to (4.26). The amount of secondary flow is given by the pitch-averaged cross momentum and displacement thicknesses, which will be used as input in the next radial flow computations (section 5).

5. MAIN PASSAGE INVISCID SECONDARY FLOWS

The ideas of the present section have been given in section 3.3. Passage averaged secondary flow momentum and continuity equations will be set up, in such a way that radial velocities will be obtained including the EWBL effects, main passage effects and main circulation changes.

The quantities which will be determined are (figure 5.1)

- (i) the inviscid passage averaged cross flow component $\tilde{w}_{u.sec.inv}$
- (ii) the difference in radial velocity between pressure and suction side $[w_n]_+^-$

$[w_n]_+^-$ contains a contribution from the end-wall boundary layers. It does not contain the blade profile boundary layer and wake radial flows which will be treated in sections 6 and 8.

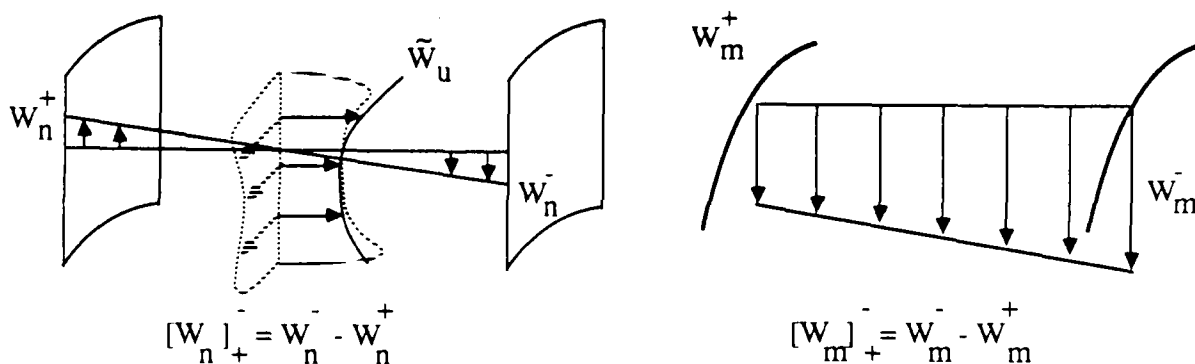


Figure 5.1 : Passage radial flow computation

5.1 Secondary flow momentum equation

The incompressible inviscid vorticity equation can be written as

$$(\vec{W} \cdot \vec{\nabla}) \cdot \vec{\omega} - (\vec{\omega} \cdot \vec{\nabla}) \cdot \vec{W} = 0 \quad (5.1)$$

The vorticity component in the n direction (see figure 3.2) will directly be assumed to be zero which means that the blade to blade flow is considered to be a potential flow.

$$\omega_n = \frac{1}{r} \frac{\partial w_m}{\partial \theta} - \frac{1}{r} \frac{\partial r w_u}{\partial m} = 0 \quad (5.2)$$

integration of eq (5.2) from pressure to suction side yields

$$\frac{1}{s} [w_m]_+^- = \frac{1}{r} \frac{\partial}{\partial m} r \bar{w}_u - \frac{\operatorname{tg} \beta}{s} [w_u]_+^- \quad (5.3)$$

$[w_m]_+^-$ represents the difference in meridional velocity between suction and pressure side of the blade (fig 5.1). s denotes the pitch. Taking the following boundary condition into account

$$w_u|_{\text{blade}} = \operatorname{tg} \beta w_m|_{\text{blade}}$$

eq (5.3) becomes

$$\frac{1}{s} [w_m]_+^- = \cos^2 \beta \frac{1}{r} \frac{\partial}{\partial m} (r \bar{w}_u) \quad (5.4)$$

The projection of equation (5.1) in the direction u is of no concern. The projection in direction m yields (see appendix A)

$$\begin{aligned} w_m \frac{\partial w_m}{\partial m} + w_n \frac{\partial w_m}{\partial n} + w_u \frac{\partial w_m}{\partial u} + w_n \left(\frac{w_n}{R_{nm}} - \frac{w_m}{R_{mn}} \right) + w_u \left(\frac{w_u}{R_{um}} - \frac{w_m}{R_{mu}} \right) \\ = w_m \frac{\partial w_m}{\partial m} + w_n \frac{\partial w_m}{\partial n} + w_u \frac{\partial w_m}{\partial u} + w_n \left(\frac{w_n}{R_{nm}} - \frac{w_m}{R_{mn}} \right) + w_u \left(\frac{w_u}{R_{um}} - \frac{w_m}{R_{mu}} \right) \end{aligned} \quad (5.5)$$

R_{ij} are the radii of curvature of the m, n, u lines (see appendix A). Expressing that

$$\begin{aligned} \omega_n &= 0 \\ R_{mu} &= 0 \\ R_{nm} &= 0 \end{aligned} \quad (5.6)$$

one finds

$$\begin{aligned} w_m \frac{\partial}{\partial m} w_m + w_n \frac{\partial}{\partial n} w_m + w_u \frac{\partial}{\partial u} w_m + w_u \frac{w_u}{R_{um}} \\ = w_m \frac{\partial}{\partial m} w_m + w_u \frac{\partial}{\partial u} w_m - w_n \frac{w_m}{R_{mn}} + w_u \frac{w_u}{R_{um}} \end{aligned} \quad (5.7)$$

Pitch averaging of this equation yields

$$\begin{aligned} \bar{w}_m \left[\frac{\partial}{\partial m} \bar{w}_m - \frac{\text{tg} \beta}{s} [\omega_m]_+^- \right] + \bar{w}_n \left[\frac{\partial}{\partial n} \bar{w}_m - \frac{\text{tg} \eta}{s} [\omega_m]_+^- \right] + \bar{w}_u \frac{1}{s} [\omega_m]_+^- + \bar{w}_u \bar{w}_u / R_{um} \\ = \bar{w}_m \left[\frac{\partial}{\partial m} \bar{w}_m - \frac{\text{tg} \beta}{s} [\omega_m]_+^- \right] + \bar{w}_u \frac{1}{s} [\omega_m]_+^- + \bar{w}_u \bar{w}_u / R_{um} - \bar{w}_m \bar{w}_n / R_{mn} \end{aligned} \quad (5.8)$$

Second order fluctuations have been neglected. η is the radial blade inclination angle which can be assumed to be very small. Assuming $\bar{w}_n \ll \bar{w}_m$ equ (5.8) reduces to

$$\begin{aligned} \bar{w}_m \frac{\partial}{\partial m} \bar{w}_m = \bar{w}_m \frac{\partial}{\partial m} \bar{w}_m + (\bar{w}_u - \text{tg} \beta \bar{w}_m) \frac{1}{s} [\omega_m]_+^- \\ - (\bar{w}_u - \text{tg} \beta \bar{w}_m) \frac{1}{s} [\omega_m]_+^- \end{aligned} \quad (5.9)$$

The second term in the r.h.s. arises from the presence of a mainflow velocity gradient (\bar{w}_u) in presence of a flow deflection ($[\omega_m]_+^-$, eq (5.4)). $[\omega_m]_+^-$ can be found from

$$[\omega_m]_+^- = \frac{1}{r} \frac{\partial}{\partial n} r [\omega_u]_+^- - \frac{\partial}{\partial u} [\omega_n]_+^- \approx \frac{1}{r} \frac{\partial}{\partial n} r [\omega_u]_+^- \quad (5.10)$$

This last contribution results from changes in circulation along the blades, since from (5.3) and (5.4)

$$\frac{1}{r} \frac{\partial}{\partial n} r [\omega_u]_+^- = \frac{1}{r} \frac{\partial}{\partial n} (s \sin \beta \cos \beta \frac{\partial}{\partial m} r \bar{w}_u) \quad (5.11)$$

Equation 5.10 is rigorous when the radial velocity is antisymmetric with u , as will be assumed below (see third step on figure 3.2).

The averages of ω_m and ω_u are given by (metric coefficients are constant with x_u)

$$\begin{aligned} \bar{\omega}_m = \frac{1}{r} \frac{\partial r \bar{w}_u}{\partial n} - \frac{1}{r} \frac{\partial \bar{w}_n}{\partial \theta} \\ \bar{\omega}_m = \frac{1}{r} \frac{\partial}{\partial n} r \bar{w}_u - \frac{1}{s} [\omega_n]_+^- \end{aligned} \quad (5.12)$$

$$\omega_u = \frac{\partial w_n}{\partial m} - \frac{\partial w_m}{\partial n} \quad (5.13)$$

$$\tilde{\omega}_u = \frac{\partial}{\partial m} \tilde{w}_n - \frac{\text{tg}\beta}{s} [w_n]_+ - \frac{\partial}{\partial n} \tilde{w}_m + \frac{\text{tg}\eta}{s} [w_m]_+ + \frac{\tilde{w}_m}{R_{mn}}$$

$1/R_{nm}$ was assumed to be small.

5.2 Superposition of secondary flows

Passage averaged quantities have been denoted with a \sim in eqs (5.3) to (5.13). Since the EWBL flows are computed separately, care must be taken with the interpretation of each of these quantities. They are to be interpreted as follows :

The meridional velocity is equal to value detained from the through flow computation.

$$\tilde{w}_m = \hat{w}_m \quad (5.14)$$

It does not include the EWBL velocity defect since it has been decided to compute the viscous layers separately.

The pitchwise velocity contains an 'inviscid' cross flow component $\tilde{w}_{u.\text{sec.}\text{inv}}$ which arises from the main non-uniformities of the flow and which is still to be determined. At this point, it is decided to superpose the cross-flow contribution from the EWBL (eq (4.7)) on \tilde{w}_u . In this way, the secondary flow information from the EWBL computation is considered as input for the present computation, in the same way as for \hat{w}_u . The recirculations arising from the EWBL which extend over the whole passage area are hence automatically included.

$$\tilde{w}_u = \hat{w}_u + \tilde{w}_{u.\text{sec.}\text{inv}} + \tilde{w}_{u.\text{sec.}\text{ewbl}} \quad (5.15)$$

5.3 Secondary flow continuity equation

Three unknown variables appear in equations (5.9) to (5.15) :

$\tilde{\omega}_m$: the passage averaged meridional secondary vorticity

$[w_n]_+^-$: the variation in radial velocity over the passage
 $w_{u.sec.inv}$: the cross flow arising from main flow non-uniformities

Closure can be obtained by means of the meridional incompressible continuity equation, written for the secondary flow velocity \vec{w}_{sec} (appendix A)

$$\frac{\partial}{\partial n} w_{n.sec} + \frac{\partial}{\partial u} w_{u.sec} - w_{n.sec} \left(\frac{1}{R_{mn}} + \frac{1}{R_{un}} \right) = 0 \quad (5.16)$$

It has been assumed that the secondary flow can be defined in the surface of constant meridional coordinate [3] and hence $w_{m.sec} = 0$. Integration of eq (5.16) over one half pitch yields

$$\frac{\partial}{\partial n} \tilde{w}_{n.sec} + \frac{2}{s} w_{u.sec}^{(m)} - \frac{1}{s} \tilde{w}_{n.sec} \left(\frac{1}{R_{mn}} + \frac{1}{R_{un}} \right) = 0 \quad (5.17)$$

where $w_{u.sec}^{(m)}$ is the mid-pitch cross flow. Equation (5.17) cannot be used without some spanwise remodeling of the secondary flow components. According to Mellor and Wood [9], the radial flow will be assumed to be linear and the pitchwise flow to be quadratic with the passage coordinate u , reducing eq (5.17) to

$$\frac{\partial}{\partial n} [w_n]_+^- \approx \frac{8}{s} \tilde{w}_{u.sec} + \frac{1}{s} [w_n]_+^- \left(\frac{1}{R_{mn}} + \frac{1}{R_{un}} \right) \quad (5.18)$$

5.4 Practical solution procedure

The secondary flow can be solved from equations (5.9), (5.12), (5.13), (5.15) and (5.18). In practice, equations (5.12), (5.15) and (5.18) are combined to (neglecting curvature for simplicity)

$$\frac{1}{8r} \frac{\partial}{\partial n} \left(rs \frac{\partial}{\partial n} [w_n]_+^- \right) = \frac{1}{s} [w_n]_+^- + \tilde{w}_m - \frac{1}{r} \frac{\partial}{\partial n} r \hat{w}_u \quad (5.19)$$

Eq (5.19) is a one dimensional second order equation with as boundary conditions a zero radial flow at hub and casing. It can easily be solved with a central difference scheme and inversion of a tridiagonal matrix.

Application in a straight cascade ($r \gg s$) would reduce eq (5.19) to

$$\frac{\partial^2}{\partial n^2} [w_n]_+ - \frac{8}{s^2} [w_n]_+ = \frac{8}{s} (\tilde{w}_m - \frac{\partial}{\partial n} \hat{w}_u) \quad (5.20)$$

which can easily be solved analytically when approaching the r.h.s. by a constant. Following analytical solution can be found in the case of a constant r.h.s.

$$[w_n]_+ = s (\partial_n \hat{w}_u - \tilde{w}_m) \left(1 - \frac{e^{an_+} e^{-an}}{e^{ah_+} e^{-ah}} \right) \quad (5.21)$$

where

$$\begin{aligned} a &= 2\sqrt{2}/s \\ h &= \text{half span} \\ n &= 0 \text{ at half span} \end{aligned} \quad (5.22)$$

Eq (5.21) is a simple result. It has been applied to the Languier Rotor test case and yields a good agreement close to that obtained by solving the full equation (5.19) (figure 9.10).

6. BLADE PROFILE BOUNDARY LAYERS

The blade profile calculation is based on an adaptation of the EWBL calculation [3]. A 2D adaptation has been introduced in the code Q3DFLO described in [1], showing a correct behaviour of the basic models used. In the present section the 3D development of the profile boundary layer is presented, which finally will yield the radial flow along the blade profiles. The theory is developed in the meridional coordinate system which is shown on figure 3.2 and discussed in appendix A.

The radial quantities will be determined from the present section are indicated on figure 6.1.

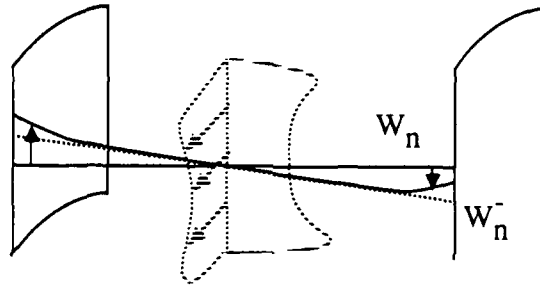


Figure 6.1 : radial flows from profile boundary layers

6.1 Momentum equations in curvilinear coordinates

In the following, the flow variables denoted with a carat $\hat{}$ are those obtained from the quasi 3D computations. The integral boundary layer approach seeks for the differences between these variables and the real flow variables.

The momentum equations will be derived taking wall curvature and variable inviscid flow parameters into account.

Both real and inviscid flow satisfy momentum conservation. Subtraction of both conservation laws yields

$$\hat{\rho}(\hat{\vec{W}}\hat{\vec{\nabla}})\hat{\vec{W}} - \rho(\vec{W}\vec{\nabla})\vec{W} + 2\omega\Lambda(\hat{\rho}\hat{\vec{W}} - \rho\vec{W}) = -\hat{\vec{\nabla}}(\hat{p}-p) + \hat{\vec{\nabla}}(-\bar{\tau}) \quad (6.6)$$

Through the use of inviscid flow parameters as reference ones, radial equilibrium is taken into account inside the PBL.

The m and n projections of the integral boundary layer momentum equation are found to be, after considerable manipulation (appendix B) :

$$\begin{aligned} & \frac{\partial}{\partial m} \rho w_m^2 (\theta_{mm} - \lambda_{mm}) + \rho w_m \delta_m^* \frac{\partial w_m}{\partial m} \\ & + \frac{\partial}{\partial n} \rho w_m^2 (\theta_{mn} - \lambda_{mn}) + \rho w_m \delta_n^* \frac{\partial w_m}{\partial n} \\ & + \frac{1}{R_{nm}} \rho w_m^2 I_{nn} + \frac{1}{R_{um}} \rho w_m^2 I_{uu} - \frac{1}{R_{mn}} \rho w_m^2 I_{mn} \pm 2\omega \frac{r}{R_{um}} \rho w_m \delta_u^* \\ & = \tau_s \end{aligned} \quad (6.7)$$

$$\begin{aligned} & \frac{\partial}{\partial m} \rho w_m^2 (\theta_{nm} - \lambda_{nm}) + \rho w_m \delta_m^* \frac{\partial w_n}{\partial m} \\ & + \frac{\partial}{\partial n} \rho w_m^2 (\theta_{nn} - \lambda_{nn}) + \rho w_m \delta_n^* \frac{\partial w_n}{\partial n} \\ & - \frac{1}{R_{nm}} \rho w_m^2 I_{mn} + \frac{1}{R_{un}} \rho w_m^2 I_{uu} + \frac{1}{R_{mn}} \rho w_m^2 I_{mm} \pm 2\omega \frac{r}{R_{un}} \rho w_m \delta_u^* \\ & = \tau_n \end{aligned} \quad (6.8)$$

where following thickness definitions are found

$$(\hat{\rho} \hat{w}_m^2)_{w_{ij}} = \int_0^\delta (\hat{w}_i - w_i) \rho w_j r d\theta \quad (6.9)$$

$$(\hat{\rho} \hat{w}_m^2)_{w_{ij}} \lambda_{ij} = \int_0^\delta (\hat{w}_{iw} - \hat{w}_i) (\hat{\rho} \hat{w}_j - \rho w_j) r d\theta \quad (6.10)$$

$$(\hat{\rho} \hat{w}_m) \delta_i^* = \int_0^\delta (\hat{\rho} \hat{w}_i - \rho w_i) r d\theta \quad (6.11)$$

$$(\hat{\rho} \hat{w}_m^2) I_{ij} = \int_0^\delta (\hat{\rho} \hat{w}_i \hat{w}_j - \rho w_i w_j) r d\theta \quad (6.12)$$

The \pm in equations (6.7) and (6.8) indicate right or left hand coordinates. The $+$ sign is selected when taking w_u always positive in the rotation sense. The thicknesses λ_{ij} which appear in eqs (6.7) and (6.8) originate from variations in velocity \hat{w} . These terms are of second order since these variations are in general small and their contribution will not be considered. Neglecting λ_{ij} reduces these equations to, after some manipulations

$$\begin{aligned} & \frac{\partial}{\partial m} \rho w_m^2 \theta_{mm} + \frac{\partial}{\partial n} \rho w_m^2 \theta_{mn} + \rho w_m \delta_m^* \frac{\partial}{\partial m} w_m + \rho w_m \delta_n^* \frac{\partial}{\partial n} w_m \\ & + \frac{1}{R_{nm}} \rho w_m (w_m \theta_{nn} - w_m \theta_{mm} + w_n \delta_n^*) - \frac{1}{R_{mn}} \rho w_m^2 (2\theta_{mn} + \delta_n^*) \\ & + \frac{1}{R_{um}} \rho w_u (w_u (\theta_{mm} + \delta_m^*) + 2U \delta_m^*) = \tau_s \end{aligned} \quad (6.13)$$

$$\begin{aligned} & \frac{\partial}{\partial m} \rho w_m^2 \theta_{nm} + \frac{\partial}{\partial n} \rho w_m^2 \theta_{nn} + \rho w_m \delta_m^* \frac{\partial}{\partial m} w_n + \rho w_m \delta_n^* \frac{\partial}{\partial n} w_n \\ & + \frac{1}{R_{mn}} \rho w_m^2 (\theta_{mm} + \delta_m^* - \theta_{nn}) - \frac{1}{R_{nm}} \rho w_m (2w_m \theta_{nm} + w_n \delta_m^*) \\ & + \frac{1}{R_{un}} \rho w_u (w_u (\theta_{mm} + \delta_m^*) + U \delta_m^*) = \tau_n \end{aligned} \quad (6.14)$$

All the variables are written in the right handed blade reference coordinate system and

$$U = \omega r \quad \text{in a rotor}$$

$$U = 0 \quad \text{in a stator}$$

For all approximations made when obtaining eqs (6.13) and (6.14) it is referred to appendix B.

Eqs (6.13) and (6.14) are to be written in the blade reference system since they are constructed from the steady Navier-Stokes equations.

6.2 Entrainment and skin friction

The entrainment equation is constructed from the continuity as follows

$$\frac{\partial}{\partial x_m} h_n h_u \rho w_m + \frac{\partial}{\partial x_n} h_m h_u \rho w_n + \frac{\partial}{\partial x_u} h_m h_n \rho w_u = 0 \quad (6.15)$$

Integration of eq (6.15) with respect to dx_u yields

$$\int_0^\delta \frac{\partial}{\partial x_m} (h_n h_u \rho w_m) dx_u + \int_0^\delta \frac{\partial}{\partial x_n} (h_m h_u \rho w_n) dx_u + [h_m h_n \rho w_u]_0^\delta = 0 \quad (6.16)$$

Inverting integral and derivative, with $\partial h / \partial x_n = 0$ and $h dx_u = r d\theta$

$$\begin{aligned} \frac{\partial}{\partial x_m} h_n \int_0^\delta \rho w_m r d\theta - [h_n r \rho w_m \frac{\partial \delta}{\partial x_m}]_0^\delta \\ + \frac{\partial}{\partial x_n} h_m \int_0^\delta \rho w_n r d\theta - [h_m r \rho w_n \frac{\partial \delta}{\partial x_n}]_0^\delta + [h_m h_n \rho w_u]_0^\delta = 0 \end{aligned} \quad (6.17)$$

Division by $h_m h_n$ and rearranging leads to

$$\begin{aligned} \frac{\partial}{\partial m} \int_0^\delta \rho w_m r d\theta - \frac{1}{R_{nm}} \int_0^\delta \rho w_m r d\theta - \rho w_m \frac{\partial \delta}{\partial m} + \rho w_m \frac{\delta}{R_{um}} \\ + \frac{\partial}{\partial n} \int_0^\delta \rho w_n r d\theta - \frac{1}{R_{mn}} \int_0^\delta \rho w_n r d\theta - \rho w_n \frac{\partial \delta}{\partial n} + \rho w_n \frac{\delta}{R_{un}} = - [\rho w_u]_0^\delta \end{aligned} \quad (6.18)$$

which is easily rearranged to

$$\begin{aligned} \frac{\partial}{\partial m} \rho w_m (\delta - \delta_m^*) + \frac{\partial}{\partial n} \rho w_n (\delta - \delta_n^*) - \frac{1}{R_{nm}} \rho w_m (\delta - \delta_m^*) - \frac{1}{R_{mn}} \rho w_n (\delta - \delta_n^*) \\ + \rho \delta \left(\frac{w_m}{R_{um}} + \frac{w_n}{R_{un}} \right) = \rho ((\vec{W} \vec{V}) \delta - [w_u]_0^\delta) \end{aligned} \quad (6.19)$$

The last term is related to the entrainment rate E as follows, s being the streamline direction

$$\begin{aligned} \rho((\vec{W}\vec{V})\delta - [w_u]_0^\delta) &= \rho \frac{w_s}{\cos\alpha} \left(\frac{\partial\delta}{\partial s} - \frac{[w_u]_0^\delta}{W} \right) \\ &= \rho \frac{w_s}{\cos\alpha \cos\beta} E \end{aligned} \quad (6.20)$$

Eq (6.20) is written in the relative coordinate system. The entrainment rate is given as an empirical function of Head's shape factor through :

$$E = 0.0306/(H^* - 3.)^{.653} \quad (6.21)$$

The validity of this empirical relation is questionable in presence of curved walls but no corrections to this equation are found in the open literature. Since it is however shown that curvature has a strong effect on the turbulence properties of the flow, it is believed that a correction should be introduced in eq (6.21). No attempts are made in the present work to correct eq (6.21) and this should be considered as a limitation in presence of strongly curved walls.

The estimation of the mainstream skin friction occurs through the use of a non dimensional skin friction coefficient generally denoted as C_f and defined through

$$\tau_s = C_f \rho \frac{\hat{w}_s^2}{2} \quad (6.22)$$

Ludwig-Tillman's relation is generally accepted. This relation expresses C_f as function of the Reynolds number and shape factor H and is originally given by

$$C_f = 0.246 \operatorname{Re}_{\theta_{ss}}^{-0.268} \exp(-1.56 H) \quad (6.23)$$

where $\operatorname{Re}(\theta_{ss})$ is defined through

$$\operatorname{Re}_{\theta_{ss}} = \frac{\hat{w}_s \theta_{ss}}{\nu} \quad (6.24)$$

As for the entrainment rate, Sumner and Shanebrook [19] analysed compressibility effects on skin friction and showed the validity of the following equation

$$C_f = 0.246 \operatorname{Re}_{\theta_{ss}}^{-0.268} \left(\frac{T_e}{T^*} \right) \exp(-1.56 H) \quad (6.25)$$

where Eckert's reference temperature T^* and the kinematic shape factor H are introduced. The reference temperature T^* for adiabatic walls is given by

$$\frac{T^*}{T_e} = 1 + 0.72 r \frac{\gamma-1}{2} M_e^2 \quad (6.26)$$

where r is the recovery factor.

Experiments show that the effect of curvature on the skin friction is not to be neglected. These experiments however indicate that the Ludwig-Tillman equation eq (6.25) is still valid. For different types of curved boundary layer flows the increase in friction and in shape factor due to curvature are related by

$$\frac{dC_f}{C_f} = - 2.5 \frac{dH}{H} \quad (6.27)$$

This behaviour is correctly predicted by the Ludwig-Tillman correlation, since from eq (6.25) it follows that

$$\frac{dC_f}{C_f} = - 1.56 H \frac{dH}{H} \quad (6.28)$$

Eqs (6.27) and (6.28) are practically equivalent for current values of H .

6.4 Profile models

Velocity profiles are introduced in order to close the system of equations. Velocity profiles and boundary layer thicknesses have been defined in meridional coordinates (figure 6.2). In this way, the orthogonality of the basic equations is conserved and all the curvature, coriolis and centrifugal contributions are found in a simple way. In analogy with the EWB profile models (section 4), following model equations are introduced :

$$\frac{w_s}{w_s} = 1 - b \left(1 - \frac{u}{\delta} \right)^n \quad (6.29)$$

$$\frac{w_n - w_s \operatorname{tg} \alpha}{w_s} = (1-b) \operatorname{tg} \epsilon'_w \left(1 - \frac{u}{\delta}\right)^n \quad (6.30)$$

where s lines are the projection of streamlines on an axisymmetric stream surface and where n lines are normal to it.

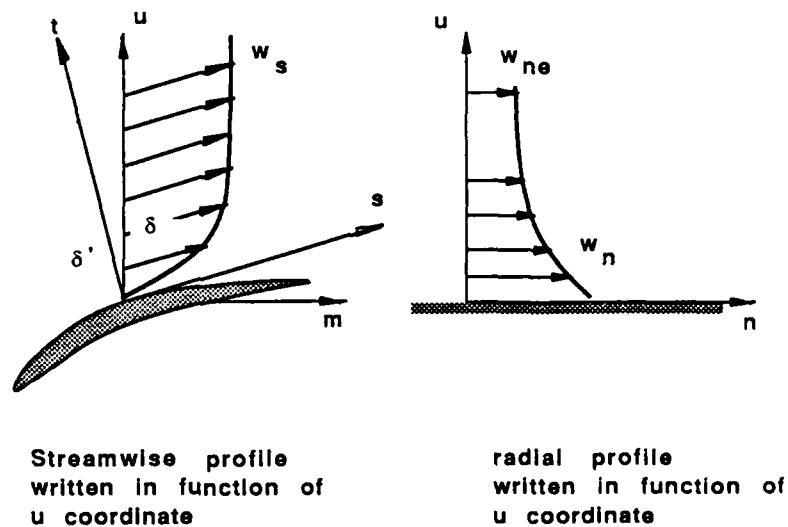


figure 6.2 : profile boundary layer
velocity profiles

The parameters b and n are correlated through the following relation [2,3]

$$b = e^{-10n\sqrt{C_f}} \quad (5.31)$$

The introduction of the model equations in the different thicknesses is detailed in appendix C.

6.5 Solution procedure

The following differential equations are considered :

- (i) the meridional momentum equation (6.13)
- (ii) the radial momentum equation (6.14)
- (iii) the entrainment equation (6.19)

Extra relations are

- (i) the entrainment rate equation (6.21)
- (ii) the friction law equation (6.23)
- (iii) the profile model equations (6.29) and (6.30),
applied in the definitions (6.9) to (6.12)

Radial momentum and displacement thicknesses are obtained, from which radial profiles can be reconstructed through the radial velocity model equation (6.12).

7. WAKE ANALYSIS

The way used by both Adkins and Smith [8] and Whitfield and Keith [30] to analyse the wake is to consider the momentum equation at the wake centerline and to assume a symmetric wake profile. Radial flows are characterised by the 'peak' radial velocity at the wake center. In the present wake approach, pressure and suction side of the wake are treated separately and the concept of 'peak velocities' is not used. The reason for this is that wake profiles may be very asymmetric. Pressure and suction side radial flows may even have opposite signs, as can be seen from the experiments of Dring [4].

The contribution to the radial flows which is obtained from the present section is shown on figure 7.1.

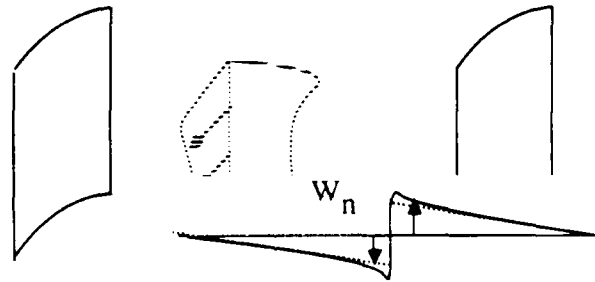


Figure 7.1 : wake radial flows

7.1 Wake profiles

The definition of the wake profiles occurs in the same way as has been done in section 6.4 for the blade profiles. The basic model equations are (see figure 7.2)

$$\frac{w_n}{w_s} = 1 - b f(n) \quad n = u/\delta = t/\delta' \quad (7.1)$$

$$\frac{w_n - w_s \tan \alpha}{w_s} = (1-b) \tan \epsilon'_w f(n) \quad (7.2)$$

The function f is shown to be close to a probability function given by

$$f(\eta) = e^{-\pi\eta^2} \quad (7.3)$$

which can be approached by [22]

$$f(\eta) = 1 - 6\eta^2 + 9\eta^3 - 3\eta^4 \quad (7.4)$$

The wake is in general considered to be symmetric, which in reality is not the case. For this reason, pressure and suction side of the wake will be considered separately and a correction in its central part will be introduced as follows, e.g. for the pressure side (+)

$$\frac{w_s^+}{w_s} = 1 - b^+ f(\eta) - (\bar{b} - b^+) g(\eta) \quad (7.5)$$

$$\frac{w_n^+ - w_s^+ \operatorname{tg} \alpha^+}{w_s} = (1 - b^+) \operatorname{tg} \epsilon^+ f(\eta) + [(1 - \bar{b}) \operatorname{tg} \bar{\epsilon} - (1 - b^+) \operatorname{tg} \epsilon^+] g(\eta) + (1 - \bar{b}) (\operatorname{tg} \bar{\alpha} - \operatorname{tg} \alpha^+) g(\eta) \quad (7.6)$$

where the correction function g chosen as

$$g(\eta) = e^{-\eta/\eta_0} \quad (7.7)$$

The + or - signs indicate pressure or suction sides. The overbars indicate mean values such as

$$\bar{b} = \frac{b^+ + b^-}{2} \quad (7.8)$$

These profiles are illustrated on figure 7.2.

The function g corrects the profile in the neighbourhood of the centerwake and makes a bridge between pressure and suction sides. At $\eta=0$, the velocities reduce to (for both sides)

$$\frac{w_s}{w_s} = 1 - \bar{b} \quad (7.9)$$

$$\frac{w_n}{w_s} = (1 - \bar{b}) (\operatorname{tg} \bar{\epsilon} + \operatorname{tg} \bar{\alpha}) \quad (7.10)$$

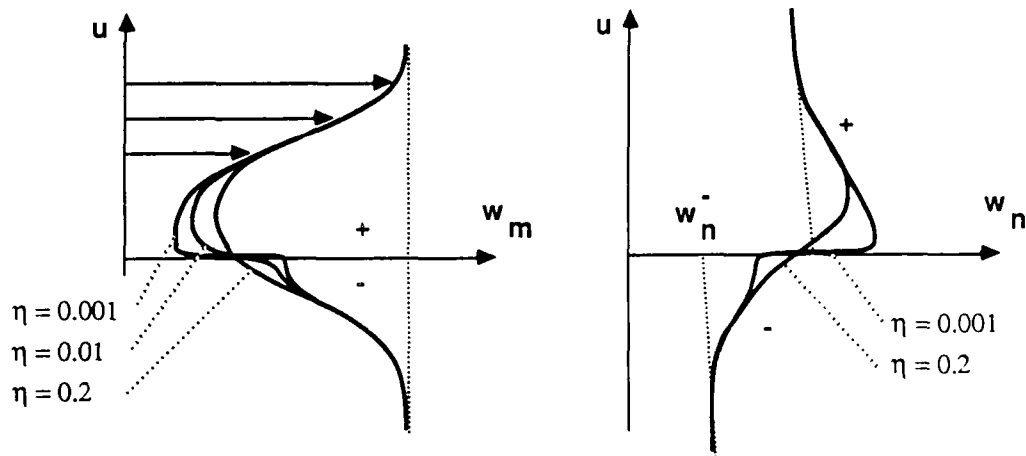


Figure 7.2 : wake profile model

For small values of η_0 , pressure and suction side of the wake conserve their identity, at higher values both sides are mixing together and the wake shape becomes more symmetric. High second derivatives are present around the centerline and the asymmetry gives rise to a diffuse mixing between pressure and suction side of the wake. Hence η_0 can be approximated by

$$\eta_0 \approx \frac{1}{\delta} \sqrt{\nu \Delta m / w_m} \quad (7.11)$$

where Δm is the distance from the trailing edge.

7.2 Integral wake momentum equations

Since pressure and suction side of the wake are considered separately, two sets of equations are used. These equations can be shown to be exactly the same as the blade momentum equations (6.13) and (6.14). Due to asymmetry, the friction terms in eqs (6.13) and (6.14) do not disappear, as

long as $b^+ \neq b^-$ and $tg\epsilon^+ \neq tg\epsilon^-$. The friction is given by (with $n=0$)

$$\begin{aligned} \frac{\tau_s^+}{\rho} &= \nu \frac{\partial w_s}{\partial t} = \nu \frac{\hat{w}_s}{\delta^+} \frac{\partial}{\partial \eta} \frac{w_s}{\hat{w}_s} \\ &= \nu \frac{\hat{w}_s}{\delta^+} \frac{1}{\eta_0} (b^- - b^+) \\ &= \nu \frac{\hat{w}_s}{\delta^+} \frac{1}{2\eta_0} (b^- - b^+) \end{aligned} \quad (7.12)$$

$$\begin{aligned} \frac{\tau_n^+}{\rho} &= \nu \frac{\partial w_n}{\partial t} = \nu \frac{\hat{w}_s}{\delta^+} \frac{\partial}{\partial \eta} \frac{w_n}{\hat{w}_s} \\ &= \nu \frac{\hat{w}_s}{\delta^+} \frac{1}{\eta_0} ((1-b^-)(tg\epsilon^- + tg\alpha^- - tg\alpha^+) - (1-b^+)tg\epsilon^+) + \tau_s tg\alpha^+ \end{aligned} \quad (7.13)$$

The pressure and suction side frictions are related by

$$\begin{aligned} \tau_s^+ &= -\tau_s^- \\ \tau_n^+ &= -\tau_n^- \end{aligned} \quad (7.14)$$

As a consequence, the friction tends to decrease the difference between momentum thicknesses at pressure and suction side.

From equations (7.4) to (7.11) it is possible to determine all the integral thicknesses, defined through eqs (6.9) and (6.11). The corresponding expressions for the wake thicknesses and their derivatives are listed in appendix D.

7.3 Local wake decay equations

The decay of the center wake velocity is determined from the center wake momentum equation which can be written as (see section 6.2)

$$\hat{\rho}(\hat{W} \cdot \hat{\nabla})\hat{W} - \rho(\hat{W} \cdot \hat{\nabla})\hat{W} + 2\hat{\omega}\Lambda(\hat{\rho}\hat{W} - \rho\hat{W}) = -\hat{\nabla}(\hat{p} - p) + \hat{\nabla}(-\bar{\tau}) \quad (7.15)$$

Assuming w_n small and $\partial_u w_m = 0$ at the wake center, the meridional component can be found from (see appendix B)

$$\begin{aligned}\vec{e}_m \cdot (\vec{W} \cdot \vec{\nabla}) \vec{W} &= w_m \frac{\partial w_m}{\partial m} + w_u \frac{\partial w_m}{\partial m} + w_u \left(\frac{w_u}{R_{um}} - \frac{w_m}{R_{mu}} \right) \\ &= w_m \frac{\partial w_m}{\partial m} + \frac{w_u^2}{R_{um}}\end{aligned}\quad (7.16)$$

$$\vec{e}_m \cdot 2\vec{\omega} \wedge \rho \vec{W} = \pm 2\omega \frac{r}{R_{um}} \rho w_u \quad (7.17)$$

$$\vec{e}_m \cdot \vec{\nabla} \bar{\tau} = \frac{\rho v}{\delta^2} \frac{\partial^2}{\partial \eta^2} w_m \quad (7.18)$$

Using eqs (7.16) to (7.18), equation (7.15) reduces to

$$\hat{w}_m \frac{\partial \hat{w}_m}{\partial m} - w_m \frac{\partial w_m}{\partial m} + (\hat{w}_u - w_u) \frac{1}{R_{um}} [(\hat{w}_u + w_u) + 2U] = - \frac{v}{\delta^2} \frac{\partial^2}{\partial \eta^2} w_m \quad (7.19)$$

Applying eq (7.5), and neglecting the curvature term for a while, one can find, for $\eta=0$ at pressure side

$$\hat{w}_m \bar{b}(2-\bar{b}) \frac{\partial \hat{w}_m}{\partial m} + \hat{w}_m^2 (1-\bar{b}) \frac{\partial \bar{b}}{\partial m} = \hat{w}_m \frac{v}{\delta^2} (b^+ f'' + (\bar{b}-b^+) g'') \quad (7.20)$$

The term in $g''(0)$ gives a discontinuity in the second derivative when going from pressure to suction side. Taking the average over both sides and equation (7.4) for f ($f''(0)=-12$) one can write, for \bar{b}

$$\frac{1}{\bar{b}} \frac{\partial \bar{b}}{\partial m} = - \frac{12v}{(1-\bar{b})\delta^2 w_m} - \frac{(2-\bar{b})}{(1-\bar{b})} \frac{1}{w_m} \frac{\partial \hat{w}_m}{\partial m} \quad (7.21)$$

where a mean value for δ is defined as

$$\frac{1}{\bar{\delta}^2} = \frac{1}{2\bar{b}} \left(\frac{b^+}{\delta^2} + \frac{b^-}{\delta^2} \right) \quad (7.21a)$$

Expressing the momentum equation (7.15) in $\eta=0$, only one equation is obtained for both sides. This equation describes the mean wake velocity defect.

In order to obtain more information about pressure and suction side mixing, a relation is searched between b^+ and b^- . This relation is obtained by writing eq (7.15) in n_1 , where n_1 is such that

$$1 = f_1 \gg g_1 \quad (7.22)$$

n_1 is a point close to the wake center but which is not influenced by the other wake side. In this way, eq (7.15) reduces to, for the pressure side and suction side

$$\hat{w}_m b^+ (2-b^+) \frac{\partial \hat{w}_m}{\partial m} + \hat{w}_m^2 (1-b^+) \frac{\partial b^+}{\partial m} = \hat{w}_m \frac{\nu}{\delta^2} (b^+ f_1'' + (\bar{b}-b^+) g_1'') \quad (7.23)$$

$$\hat{w}_m b^- (2-b^-) \frac{\partial \hat{w}_m}{\partial m} + \hat{w}_m^2 (1-b^-) \frac{\partial b^-}{\partial m} = \hat{w}_m \frac{\nu}{\delta^2} (b^- f_1'' + (\bar{b}-b^-) g_1'')$$

and, taking the difference, with $\Delta b = b^+ - b^-$

$$\hat{w}_m^2 (1-\bar{b}) \Delta b \frac{\partial \hat{w}_m}{\partial m} + \hat{w}_m^2 (1-\bar{b}) \frac{\partial \Delta b}{\partial m} - \hat{w}_m^2 \Delta b \frac{\partial \bar{b}}{\partial m} = \hat{w}_m \frac{\nu}{\delta^2} \Delta b (f_1'' - g_1'') \quad (7.24)$$

Hence,

$$\frac{\partial \Delta b}{\partial m} = - \frac{\nu \Delta b}{\delta^2 \hat{w}_m (1-\bar{b})} (g_1'' - f_1'') + \frac{\Delta b}{(1-\bar{b})} \frac{\partial \bar{b}}{\partial m} - 2 \Delta b \frac{1}{\hat{w}_m} \frac{\partial \hat{w}_m}{\partial m} \quad (7.25)$$

and taking eqs (7.4) and (7.7) for f and g yields, with eq (7.22)

$$\frac{1}{\Delta b} \frac{\partial \Delta b}{\partial m} = - \frac{12 \nu}{\delta^2 \hat{w}_m (1-\bar{b})} + \frac{1}{(1-\bar{b})} \frac{\partial \bar{b}}{\partial m} - \frac{2}{\hat{w}_m} \frac{\partial \hat{w}_m}{\partial m} \quad (7.26)$$

In a very similar way, by considering the projection of eq (7.15) in the n direction, one can find

$$\frac{1}{\Delta(tg\alpha + tg\epsilon)} \frac{\partial}{\partial m} \Delta(tg\alpha + tg\epsilon) = - \frac{12 \nu}{\delta^2 \hat{w}_s (1-\bar{b})} - \frac{1}{\hat{w}_s} \frac{\partial \hat{w}_s}{\partial m} \quad (7.27)$$

Eqs (7.26) and (7.27) close the system of wake equations, the only unknown left is the eddy viscosity coefficient ν which is obtained from

$$v = K \delta b w_m$$

(7.28)

The coefficient K is to be calibrated.

7.4 Practical solution procedure

Six independent variables are present in the wake equations :

δ^+, δ^- : pressure and suction side wake thickness
 b^+, b^- : pressure and suction side wake velocity defect
 ϵ^+, ϵ^- : pressure and suction side skewing angle

Closure is obtained with the following differential equations :

pressure and suction side eqs (6.13) :

integral meridional momentum expressed at
 pressure and suction side

sum of pressure and suction side eq (6.14) :

sum of the integral radial momentum expressed at
 pressure and suction side

equation (7.21) : local meridional momentum equation along wake center

equation (7.26) : difference between local meridional momentum
 equations expressed at pressure and suction side

equation (7.27) : difference between local radial momentum
 equations expressed at pressure and suction side

The two radial momentum equations (6.14) could be considered at pressure and suction side separately, making equation (7.27) redundant. In practice, numerical instability was however observed when using the radial momentum equations separately at pressure and suction side. This instability is due to singularities in the Jacobian matrix which relates the momentum thicknesses with the wake parameters b, δ and $t g \epsilon$. In particular, it was found that the profile model equations are not very sensitive to the difference $\Delta t g \epsilon$ and the radial momentum equation (6.14) has therefore been expressed over the whole wake. This equation mainly controls the mean

skewing $\tan \bar{\epsilon}$ and τ_n disappears from the system of equations. Equation (7.13) for τ_n is not used.

New parameters which appear in these equations are the integral wake momentum and displacement thicknesses, the central wake shear stress τ_s , a mixing length n_0 and a diffusion coefficient ν . These extra parameters are found from

equations (7.5) and (7.6) : wake velocity models which allow the determination of the integral wake thicknesses

equation (7.12) : stress from the model equations

equation (7.11) : model for the mixing length ν_0

equations (7.28) : model for the diffusion coefficient ν

The meridional profiles are modeled by δ^+ , δ^- , b^+ , b^- . These variables are the main parameters of the two meridional integral equations (6.13) and meridional local equations (7.21) and (7.26). The radial profiles are modeled by the skewing angles ϵ^+ and $\bar{\epsilon}$. The difference $\Delta \tan \epsilon$ is controlled by the extra equation (7.27).

8. TRAILING EDGE AND NEAR WAKE

The wake equations as discussed in section 7 are not directly applicable in a region very close to the trailing edge, mainly because of the presence of strong pressure gradients which are not considered in the momentum equations (6.13) and (6.14). A detailed description inside this region is not considered, since the complexity of the computation is not in proportion to the gain in information. Direct jump relations between the momentum and displacement thicknesses at trailing edge and downstream wake are therefore searched.

These relations are based on work of Kool and Hirsch [20]. The pressure recovery from trailing edge to the downstream wake center is proposed as [20]

$$C_p = 0.3 (1 - 56 C_q) \quad (8.1)$$

where

$$C_p = \frac{p^{\text{tot}} - p_{te}^{\text{tot}}}{\rho W^2 / 2} \quad (8.2)$$

$$C_q = \frac{\theta_{te}}{x_R + x_0} \quad (8.3)$$

$$x_0 \approx 81 \theta_{te} \quad (8.4)$$

$$x_R \approx 5.6 r_{te}$$

R = downstream stagnation point

te = trailing edge

Application of these relations in the wake momentum equations yields [20]

$$\theta_R \approx 1.45 \theta_{te} + 0.1 r_{te} \quad (8.5)$$

It is clear that this relation cannot be valid for the complete range of the ratio r_{te}/θ_{te} . For very small trailing edge radii, one should in the limit find

$$\theta_R \approx \theta_{te} \quad (8.6)$$

8. TRAILING EDGE AND NEAR WAKE

The wake equations as discussed in section 7 are not directly applicable in a region very close to the trailing edge, mainly because of the presence of strong pressure gradients which are not considered in the momentum equations (6.13) and (6.14). A detailed description inside this region is not considered, since the complexity of the computation is not in proportion to the gain in information. Direct jump relations between the momentum and displacement thicknesses at trailing edge and downstream wake are therefore searched.

These relations are based on work of Kool and Hirsch [20]. The pressure recovery from trailing edge to the downstream wake center is proposed as [20]

$$C_p = 0.3 (1 - 56 C_q) \quad (8.1)$$

where

$$C_p = \frac{p^{\text{tot}} - p_{\text{te}}^{\text{tot}}}{\rho W^2 / 2} \quad (8.2)$$

$$C_q = \frac{\theta_{\text{te}}}{x_R + x_0} \quad (8.3)$$

$$x_0 = 81 \theta_{\text{te}} \quad (8.4)$$

$$x_R = 5.6 r_{\text{te}}$$

R = downstream stagnation point

te = trailing edge

Application of these relations in the wake momentum equations yields [20]

$$\theta_R = 1.45 \theta_{\text{te}} + 0.1 r_{\text{te}} \quad (8.5)$$

It is clear that this relation cannot be valid for the complete range of the ratio $r_{\text{te}}/\theta_{\text{te}}$. For very small trailing edge radii, one should in the limit find

$$\theta_R = \theta_{\text{te}} \quad (8.6)$$

Experiments [20] indicate that eq (8.5) is valid from $r_{te}/\theta_{te} = 10$ on. For lower ratio's a simple linear interpolation between eqs (8.5) and (8.6) is proposed through

$$\theta_R = \theta_{te}(1+0.045r_{te}) + .01 r_{te}/\theta_{te} \quad (8.7)$$

The momentum thickness is not sufficient as information to determine the wake profile downstream of the near wake region. According to Kool and Hirsch [20], one should take b close to 1 according to the existence of a stagnation point inside the near wake. b should however not be regarded as the real velocity defect, but rather as a parameter in the model equation eq (7.1). This parameter probably deviates from its physical meaning in the near wake and it controls the whole outer wake, where the profile boundary layer history is still strongly present. For these reasons, it is proposed to keep the physical thickness δ as a constant value in the jump over the trailing edge, rather than imposing an arbitrary value for b .

A third jump relation is required for the radial flow thicknesses. Assuming no particularities in the radial pressure gradient in the near wake, one can assume the radial momentum to be constant.

In conclusion, the jump relations can be written as

$$\begin{aligned} \theta_{mm} &= f(\theta_{mm,te}, r_{te}) \\ \delta &= \delta_{te} \\ \theta_{nn} &= \theta_{nn,te} \end{aligned} \quad (8.8)$$

where eq (8.5) or (8.7) apply for the first relation

9. RESULTS

Three test cases were considered at present : an isolated airfoil wake which is two dimensional [23], the Languier rotor [5] and the Dring rotor [4].

9.1 Isolated airfoil [23]

The isolated airfoil case is used to test the wake equations in the two-dimensional case for both symmetric and asymmetric flow behaviour. The airfoil is a NACA-0012 airfoil, experiments are available at 0° , 5° and 10° angle of attack. Results are shown on figures 9.1 to 9.6. Figures 9.1, 9.3 and 9.5 compare the experimental and the computed wake displacement and momentum thicknesses, on figures 9.2, 9.4 and 9.6 the corresponding wake velocity profiles are shown. The wake thicknesses are compared separately for the pressure side, suction side and total wake. The asymmetric results show the correct transfer of momentum from the thicker suction side to the thinner pressure side of the wake (figures 9.3 and 9.5). The transfer of momentum occurs only through the shear stress τ_s which is computed from equation (7.12), indicating a correct estimation of n_0 through equation (7.11). The coefficient K is found to be 0.01.

The wake profiles (figures 9.2, 9.4, 9.6) show the correct behaviour of the model equations (7.4) to (7.7) for downstream positions of 5, 10 and 20 % chord distance from the trailing edge. At shorter distances 0.7 and 2 % chord, a better agreement cannot be found since the wake profiles are still closer to the boundary layer profile shapes than to the Gaussian wake shape. Attempts to define a transition region in the near wake were undertaken, but the gain in information is not in proportion to the increase of complexity required. The transition region between profile boundary layer and wake computations is rather to be bypassed by the use the jump relations 8.8.

9.2 ONERA rotor [5]

The ONERA rotor has been considered as a test case for radial mixing computations by several authors [8,30]. Results are presented near the mean diameter at 30 % axial chord distance downstream of the trailing edge. The blades have radially constant solidity and no twist, giving rise to a substantial central secondary flow.

The results presented in this section are obtained by a full computation, without any input from the experimental data. The ONERA rotor was treated by a Quasi 3D code which yields all the input required to run the EWBL, main passage secondary flow, Profile Boundary Layers and wake computations.

The new elements which are tested at this level are the profile boundary layer computations which result in the entry conditions of the wake computations, and main secondary flow equations 5.9 and 5.18.

The result obtained at trailing edge is shown on figure 9.7. It is to be observed that the radial velocities observed in the Languier rotor are mainly due to its non-free vortex design. The contribution from EWBL and profile boundary layer secondary flows is very small, as can be seen from figure 9.8 where the vorticity ω_m was taken zero.

Figures 9.9 and 9.10 compare the experimental wake profiles with computed results. The differences between computation and experiment lie within the differences observed in [5] when different types of anemometers are used.

9.3 Dring rotor [4]

Extensive measurements were made by Dring et al [4] downstream of a single rotor blade row. Velocity measurements are available at four downstream stations, at several radii. Measurements were made at four different flow rates.

It is the aim of the present work to predict these results through a total computation (Quasi3D, EWBL, PBL, central secondary flow, wake). The profile boundary layer computations however predict trailing momentum thicknesses which are far too small (7 to 10 times the observed values) and at present this problem has not yet been solved. The underestimation is due either to an inaccurate estimation of the velocity gradients along the profiles, either to the presence of separations near the trailing edge, which may cause a momentum loss which is much larger than the one predicted through eq (8.5).

At present, the testing of the Dring rotor is therefore limited to the 3D wake computation, using the first experimental station data as input.

Results are presented at two different flow rates ($\phi = 0.65$ and $\phi = 0.85$) on figures 9.11 and 9.12. These figures compare the obtained meridional and

radial flow velocities with Dring's data, at three radii. The lowest flow rate is close to the stall limit, whereas the higher one gives a certain amount of secondary flow due to non-free vortex behaviour. A quite good agreement is in general observed. The value for the dispersion coefficient K in eq (6.23) was however to be increased considerably for the test case close to the stall limit, which can be explained only by an important increase in turbulence.

A strong radial flow is observed experimentally inside the wake close to the stall limit. Such a strong radial flow is not found when applying the profile boundary layer equations. It is probably due to separations in the neighbourhood of the trailing edge, causing a stronger wake centrifugation at this place, as stated by Dring et al.

The total radial recirculation due to the non-free vortex behaviour at the higher flow rate appears to be more important than the wake radial flow itself, indicating that strong radial mixing effects are to be expected in off-design conditions.

CONCLUSIONS

The main tools required for the prediction of the radial flow distributions in a compressor stage have been developed in the present report. This theory is based on the superposition of the different contributions from end-wall boundary layers, profile boundary layers, wakes and main passage secondary flows. All the viscous aspects are treated by an integral approach where velocity profile models are introduced. The inviscid secondary flow behaviour is obtained from pitch averaged vorticity and continuity equations.

The behaviour of the asymmetric wake and of the central inviscid secondary flows are well verified by experiments. The behaviour of the EWBL flows are treated elsewhere [2,3]. The profile boundary layers is applied in the Languier test case, where a full computation has been done. No direct comparison is made for the Profile boundary layers however.

Strong radial flows are induced by a non-free vortex behaviour, indicating possible strong radial mixing effects in off-design conditions. Strong radial flows are also observed in the wake, close to the stall limit, these strong radial flows are not predicted by the profile boundary layers equations in the present state of the project.

In the present state, the theory which has been developed seems to be able to predict the radial flow in a reliable way when no important separations occur, as can be expected at design conditions. In this situation radial recirculations should be due mainly to the EWBL and PBL cross flows. Through the approach which has been used, all the secondary flow aspects are implicitly or explicitly present in the radial flow prediction, including effects such as a tip clearance through the EWBL theory.

FUTURE WORK

The main part of the radial mixing theory lies in the prediction of the radial flow intensity, which implies a total knowledge of the secondary flows in a turbomachine.

Each aspect of this secondary flow prediction is to be tested separately, which has not been done for the profile boundary layers equations yet. Recently detailed Profile Boundary Layers experimental data have been made available [24,25] and a separate testing of the profile boundary layers will be performed.

Once the radial flows known, the mixing process itself can be described. The main difficulty is to balance the contributions radial mixing due to convection and mixing due to turbulent diffusion when calibrating the two contributions. This will be analyzed in the final report.

References

- [1] HIRSCH C., WARZEE G., 1979, "An Integrated Quasi-3D Finite Element Calculation Program for Turbomachinery flows" ASME Journal of Engineering for Power, Vol 101, pp 141-148.
- [2] DE RUYCK J., 1982, "Computation of End-Wall Boundary Layers in Axial Compressors" Phd Thesis, Vrije Universiteit Brussel, Dept of Fluid Mechanics.
- [3] DE RUYCK J., HIRSCH C., 1983, "End-Wall Boundary Layers in Multistage Axial Compressors" AGARD 61 th Specialist Meeting, Viscous Effects in Turbomachines, CP .
- [4] DRING R.P., JOSLYN H.D., HARDIN L.W., 1982, "An Investigation of Axial Compressor Rotor Aerodynamics" ASME J. Eng. for Power, vol 104, pp 84-94, jan 1982.
- [5] LARGUIER R., 1980, "Experimental Analysis Methods for Unsteady Flows in Turbomachines" Measurement Methods in Rotating Components of Turbomachinery, P71, ASME.
- [6] GALLIMORE S.J., CUMPSTY N.A., "Spanwise Mixing in Multistage Axial Flow Compressors : Part I - Experimental Investigation" ASME paper 86-GT-20.
- [7] GALLIMORE S.J., "Spanwise Mixing in Multistage Axial Flow Compressors : Part II - Throughflow Calculations Including Mixing" ASME paper 86-GT-21.
- [8] ADKINS G.G., SMITH L.H., 1982, "Spanwise Mixing in Axial-Flow Turbomachines" ASME J. of Eng. for Power, vol 104, pp 97-110.
- [9] MELLOR G.M., WOOD G.L., 1971, "An Axial Compressor End-Wall Boundary Layer Theory" ASME Journal of Basic Engineering, Series d, Vol 93, pp 300-316.
- [10] Balsa T.F., MELLOR G.L., 1975, "the Simulation of Axial Compressor Performance Using an Annulus Wall Boundary Layer Theory" ASME Journal of Engineering for Power, pp 305-318.
- [11] SMITH L.H., 1955, "Secondary Flow in Axial-Flow Turbomachinery" Trans. ASME, Vol 77, no 7, p 1065.

- [12] HAWTHORNE W.R., 1951, "Secondary Circulation in Fluid Flow" Proc. Roy. Soc. Vol a, no 209, pp 374-;397.
- [13] SMITH A.G., 1957, "On the Generation of the Streamwise Component of Vorticity for Flows in Rotating Passages" Aeronaut. Quart. 8 : 369.
- [14] DIXON S.L., 1974, "Secondary Vorticity in Axial Compressor Blade Rows" Nasa Sp304.
- [15] COOKE, HALL, 1962, "Boundary Layers in Three Dimensions" Progress in Aeronautical Sciences, Vol 2, Boundary Layer Problems, Pergamon.
- [16] HORLOCK J.H., 1971, "Cross Flows in Bounded Three Dimensional Turbulent Boundary Layers" Cambridge U., Cued/a -; Turbo/tr28.
- [17] SMITH L.H., 1969, "Casing Boundary Layers in Multistage Axial Flow Compressors" Brown Boveri Symposium, Flow Research on Blading, Elsevier.
- [18] HORLOCK J.H., PERKINS H.J., 1974, "Annulus Wall Boundary Layers in Turbomachines" Agard ag 185.
- [19] SUMNER W.J., SHANEBROOK J.R., 1972, "Entrainment Equation for Three-Dimensional Compressible Turbulent Boundary Layers" AIAA Journal, Vol 10, no 5 pp 693-694.
- [20] KOOL P., HIRSCH CH., 1982 "A Prediction scheme for the Decay of a Turbomachine blade wake" ASME paper nr 82-GT-273.
- [21] WHITFIELD C.W., KEITH J.S., 1985 "Spanwise Redistribution of Energy and Loss in an Axial Flow Compressor by Wake Centrifugation", AFWAL report TR-84-2109, Wright Patterson Air Force Base.
- [22] KORKAN K.D., PETRIE S.L., GASPERAS G., 1977 "A Unified Theory of the Two Dimensional and Axisymmetric Laminar, Transition and Turbulent Wake Process Utililizing the Integral Technique", AIAA paper 77-708.
- [23] DE RUYCK J., HIRSCH C., "Instantaneous Turbulence Profiles in the Wake of an Oscillating Airfoil" AIAA Paper 82-0353, 1982.
- [24] LAKSHMINARAYANA B., POPOVSKI P. "Three-Dimensional Boundary Layer on a Compressor Rotor Blade at Peak Pressure Rise Coefficient" ASME Journal of Turbomachinery, Vol 109, pp 91-98, january 1987.

- [25] AGARD report on "Computation of Three-Dimensional Boundary Layers Including Separation" AGARD report 741, April 1986.
- [26] CARTER, COHEN "Preliminary Investigation into the Three-Dimensional Flow through a Cascade of Aerofoils", Aero. Res. Council, R & M 2336, 1946.
- [27] SQUIRE H.B., WINTER K.G. "The Secondary Flow in a Cascade of Airfoils in a Nonuniform Stream" Journal of Aeronaut. Sc., Vol 18, p271, 1951.
- [28] HAWTHORNE W.R., "Rotational flow through Cascades" Q. Jl. Mech. appl. Math. Vol 8, part 3, pp 266-292, 1955.
- [29] CAME P.M., MARSH H., "Secondary Flow in Cascades : two Simple Derivations for the Components of Vorticity", Jl. Mech. Eng. Sci., Vol 16, No 6, pp 391-401, 1974.
- [30] WHITFIELD C.W., KEITH J.S., "Spanwise Redistribution of Energy and Loss in an Axial Flow Compressor by Wake Centrifugation", Wright Patterson Air Force Base, OHIO 45433, Final report AFWAL-TR-84-2109, 1984.
- [31] HAH C., LAKSHMINARAYANA B., "Prediction of Two- and Three- Dimensional Asymmetrical Turbulent Wakes, Including Curvature and Rotation Effects" AIAA Journal Vol 18, No 10, 79-1561, 1979.
- [32] RAVINDRANATH A., LAKSHMINARAYANA B., "Mean Velocity and Decay Characteristics of the Near and Far Wake of a Compressor Rotor Blade of Moderate Loading" Trans. ASME, Journal of Engineering for Power, Vol 102, pp 535-548, 1980.
- [33] REYNOLDS B., LAKSHMINARAYANA B., "Characteristics of Lightly Loaded Fan Rotor Blade Wakes" NASA CR-3188, 1979.
- [34] BURDSALL E.A., CANAL E.Jr., LYONS K.A., "Core Compressor Exit Stage Study - I. Aerodynamic and Mechanical Design", NASA CR-159714, PWA-5561-55, 1979.
- [35] BEHLKE R.F., BURDSALL E.A., CANAL E.Jr, Korn N.D., "Core Compressor Exit Stage Study - II. Final report", NASA CR-159812, PWA-5561-66, 1979.

ISOLATED NACA 0012 AIRFOIL WAKE zero degree angle of attack

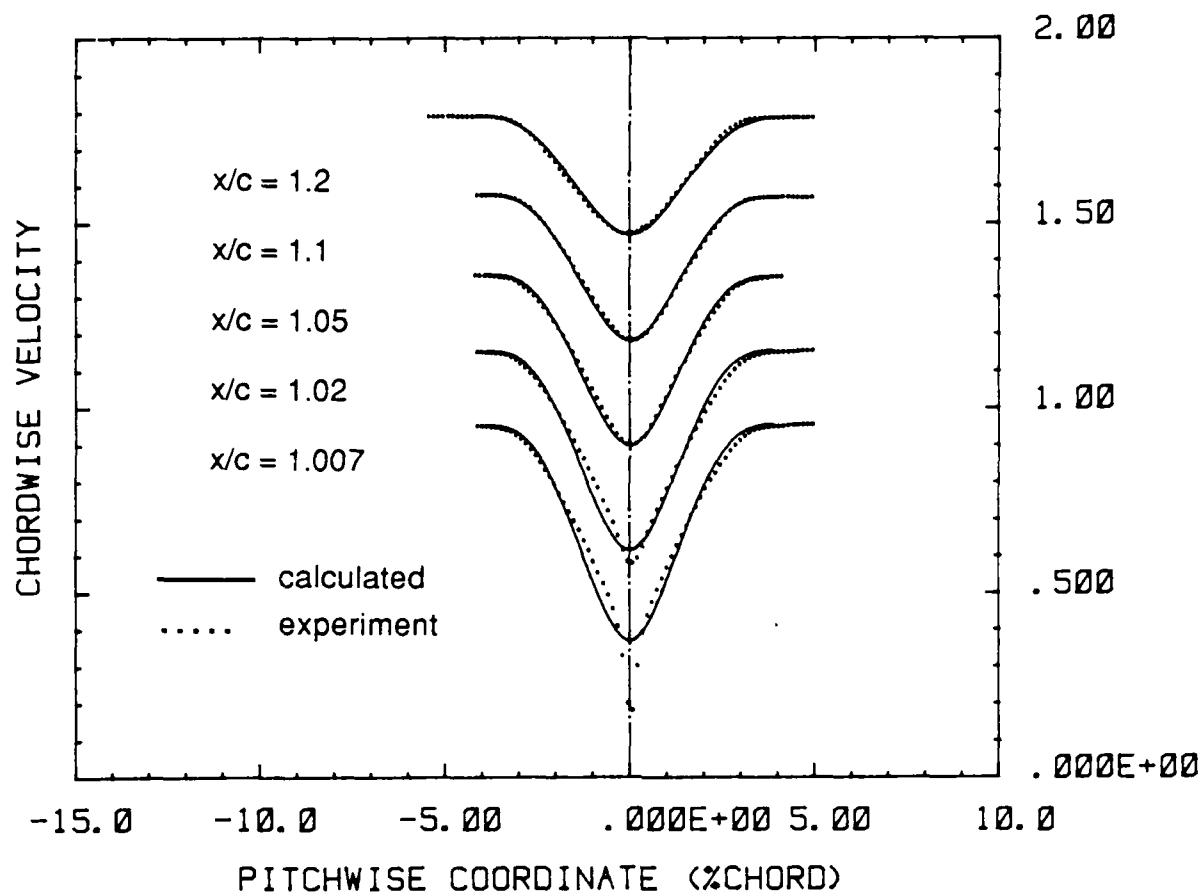


FIGURE 9.2

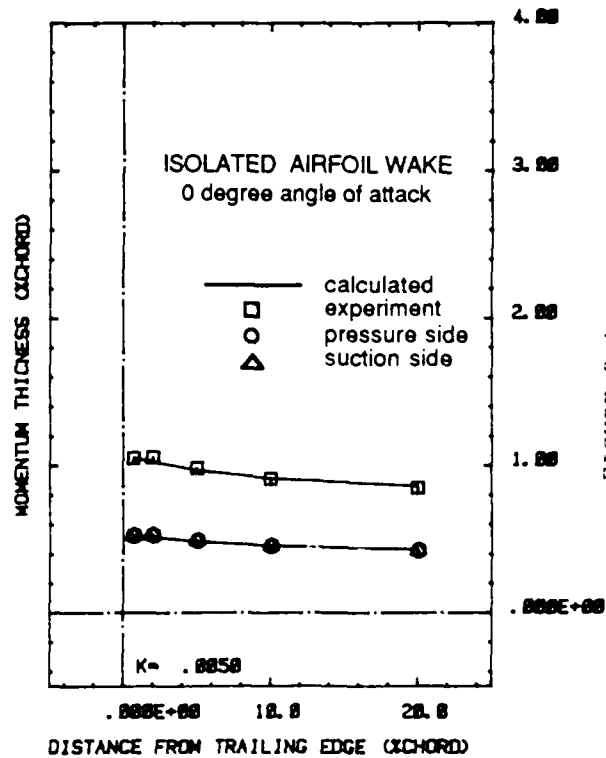
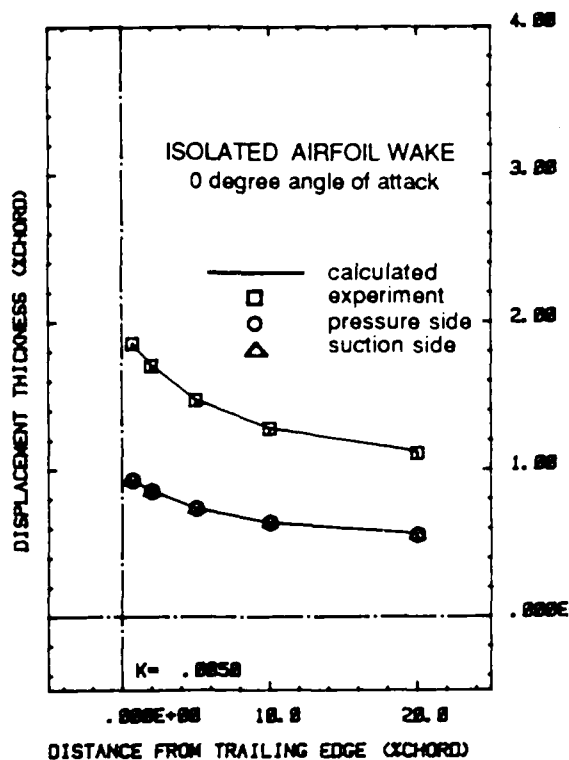


FIGURE 9.1

ISOLATED NACA 0012 AIRFOIL WAKE 5 degree angle of attack

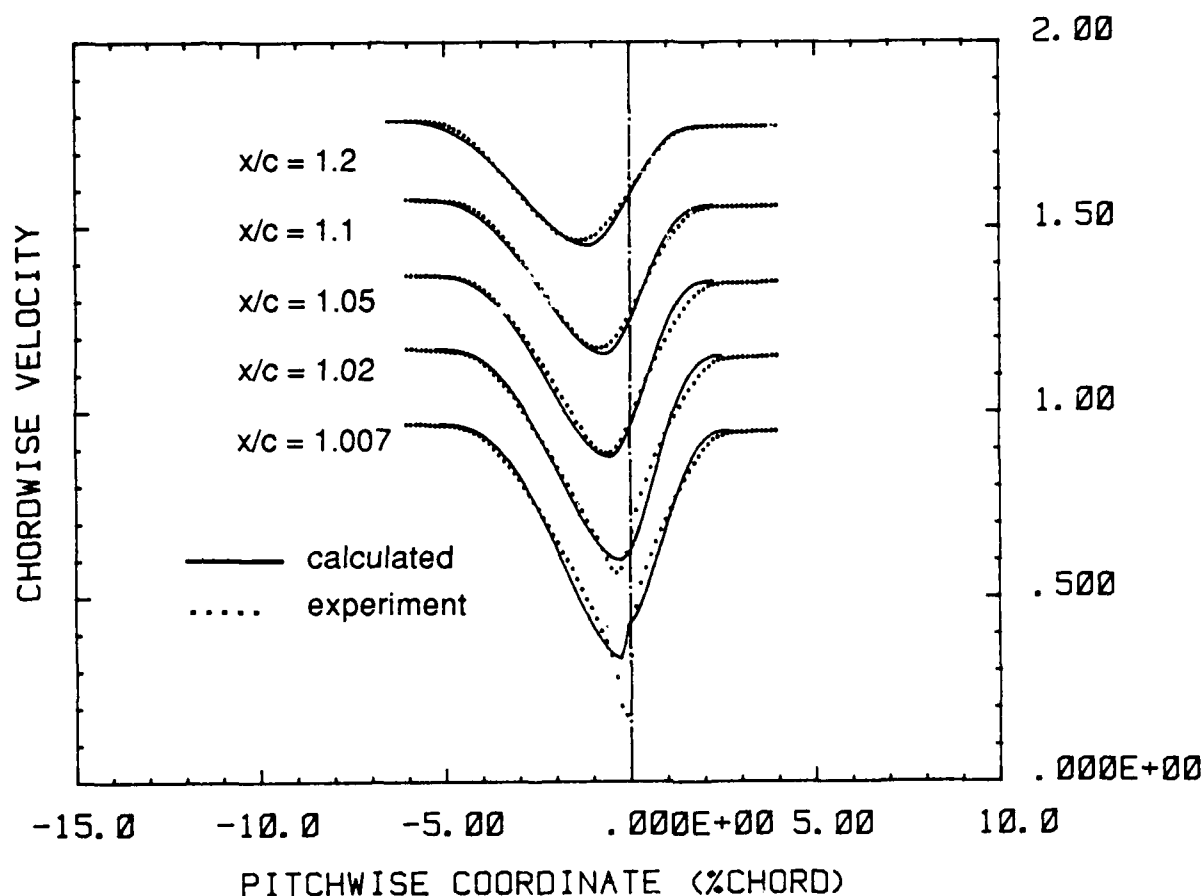


FIGURE 9.4

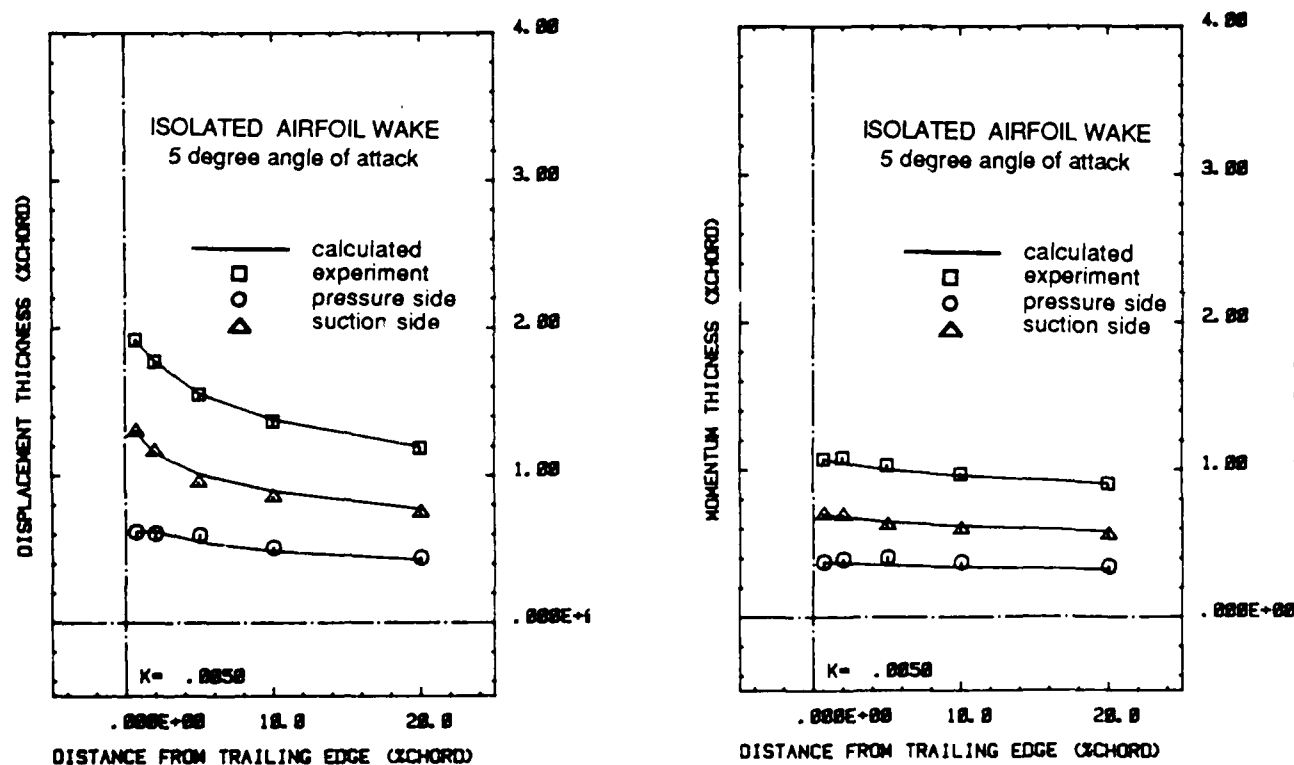


FIGURE 9.3

ISOLATED NACA 0012 AIRFOIL WAKE 10 degree angle of attack

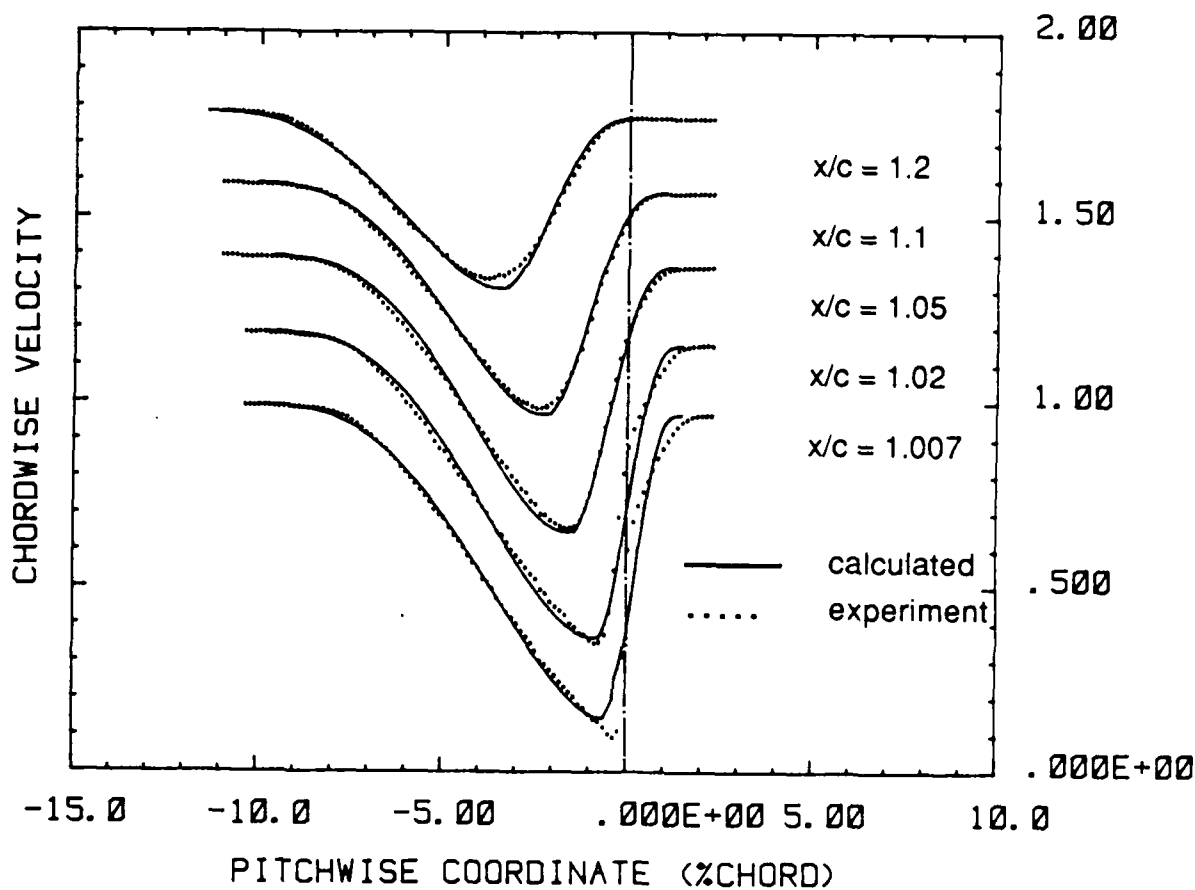


FIGURE 9.6

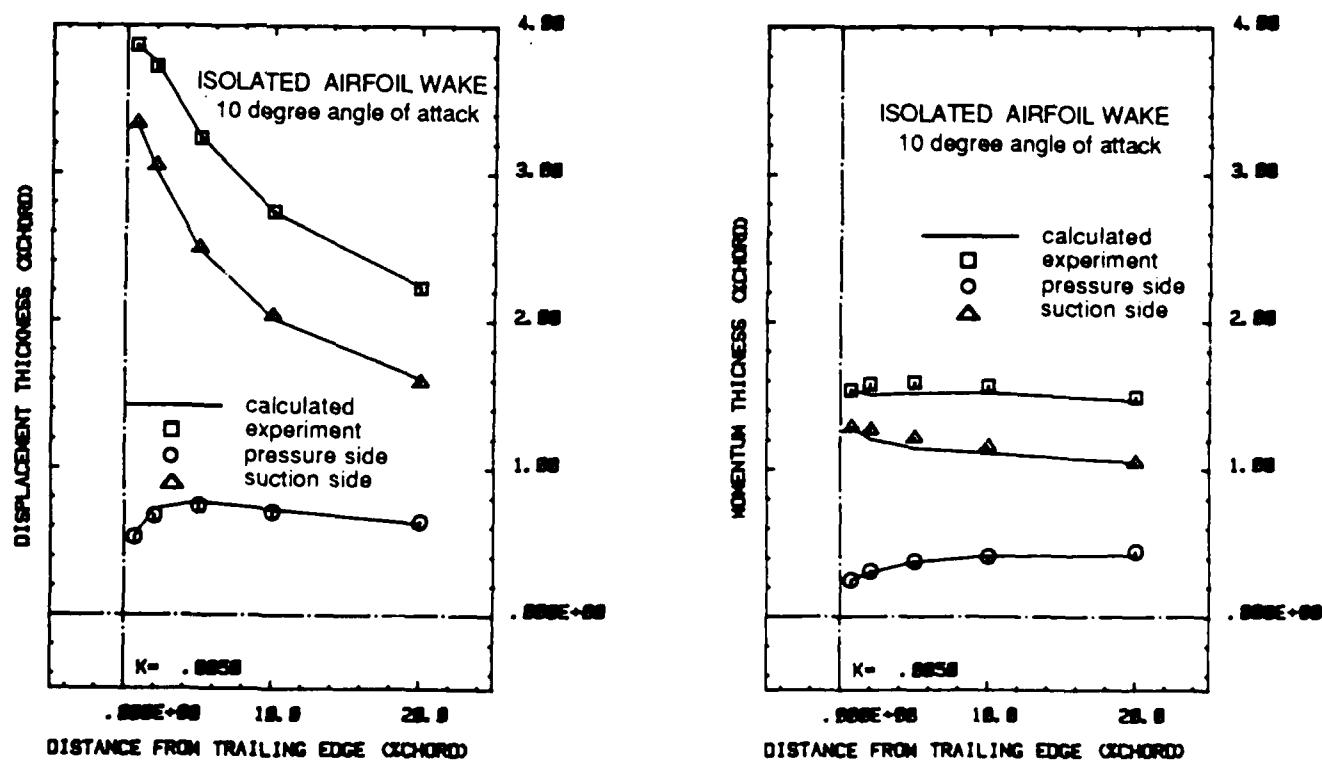


FIGURE 9.5

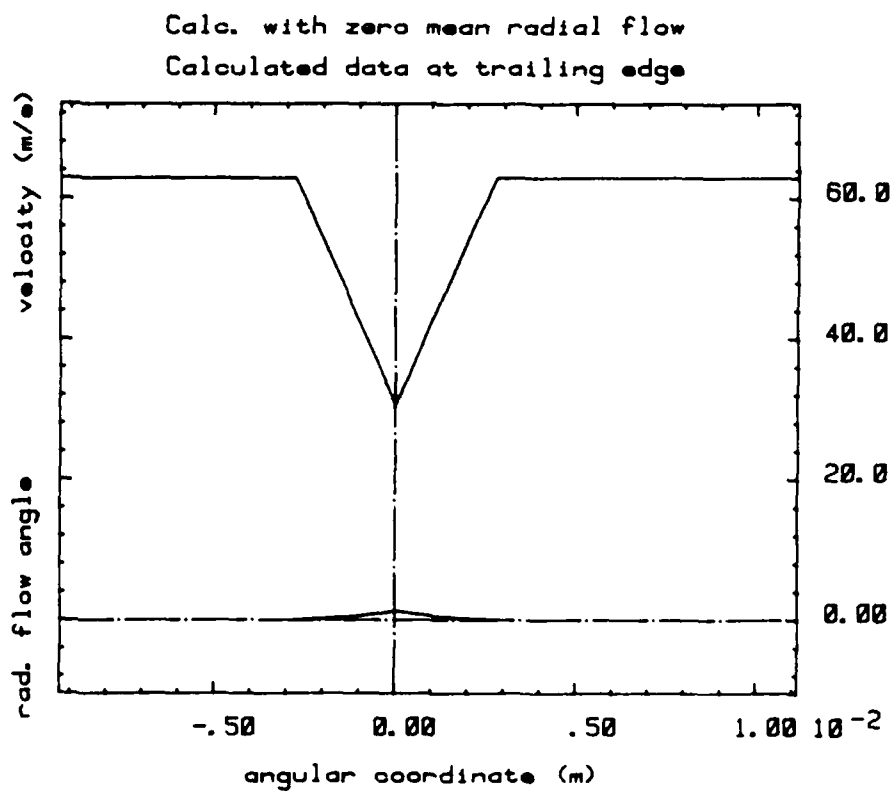
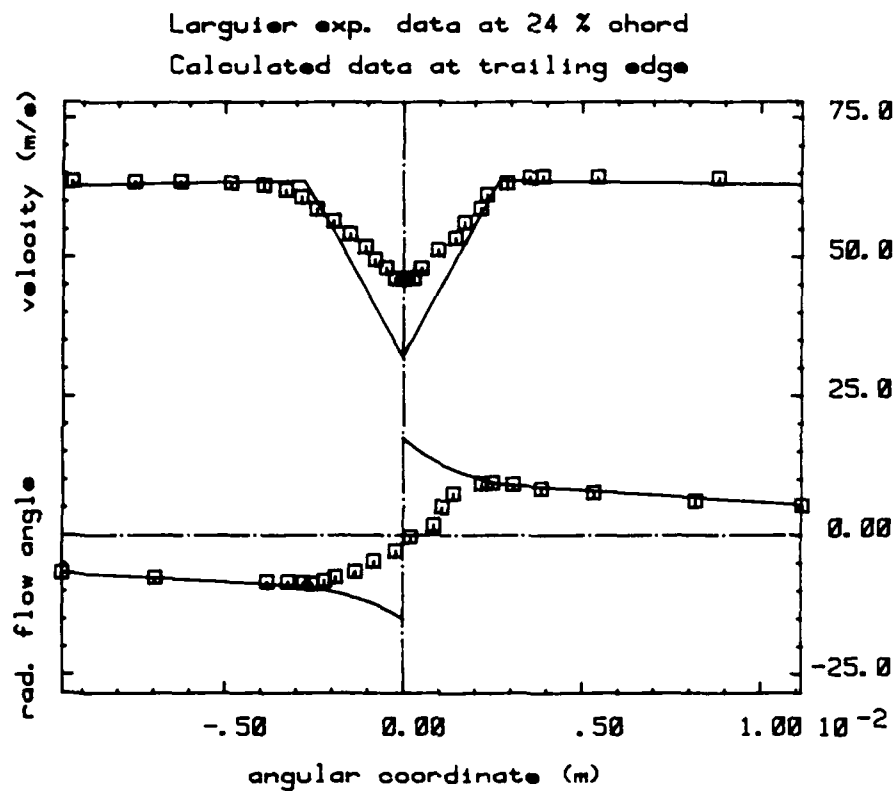


FIGURE 9.8

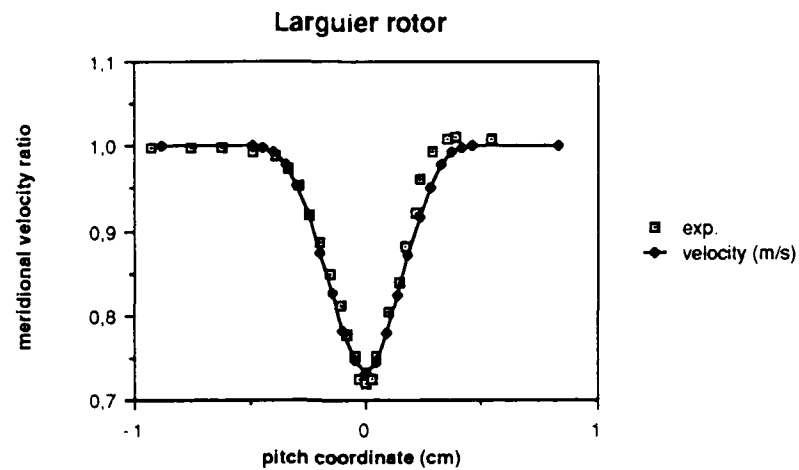


Figure 9.9

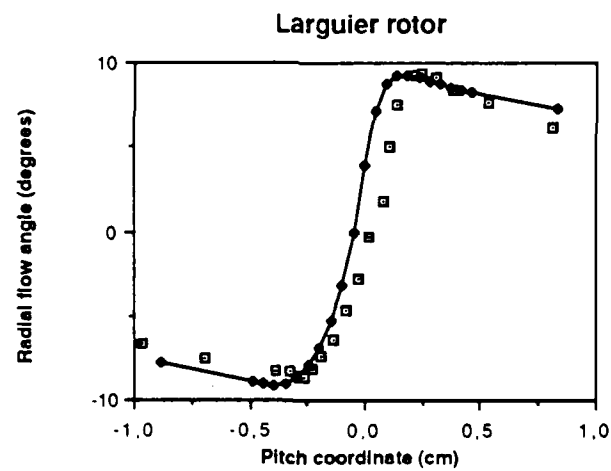
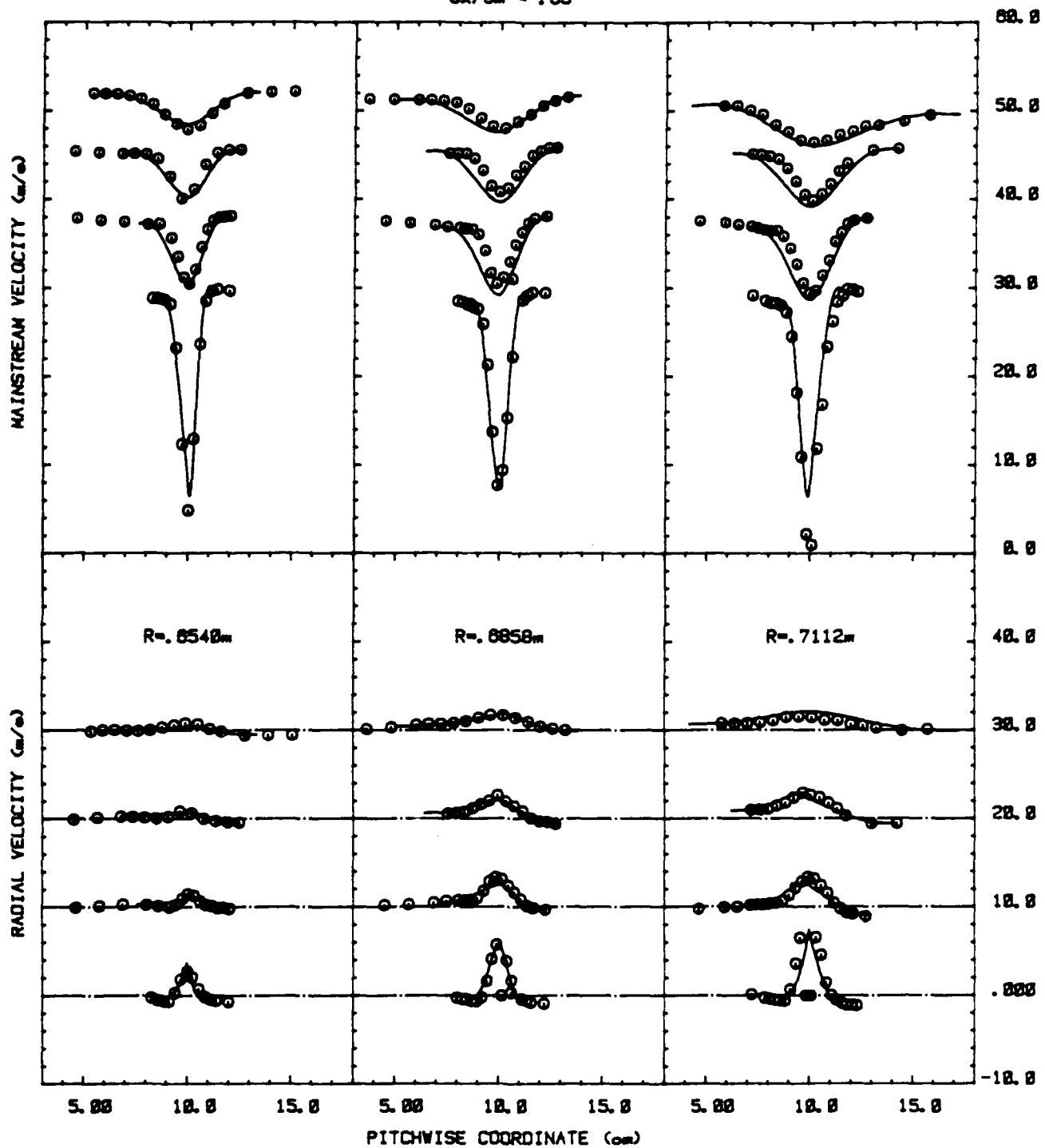


Figure 9.10

DRINGROTOR
 $C_x/U_m = .85$



○ experimental
 - predicted

Figure 9.11

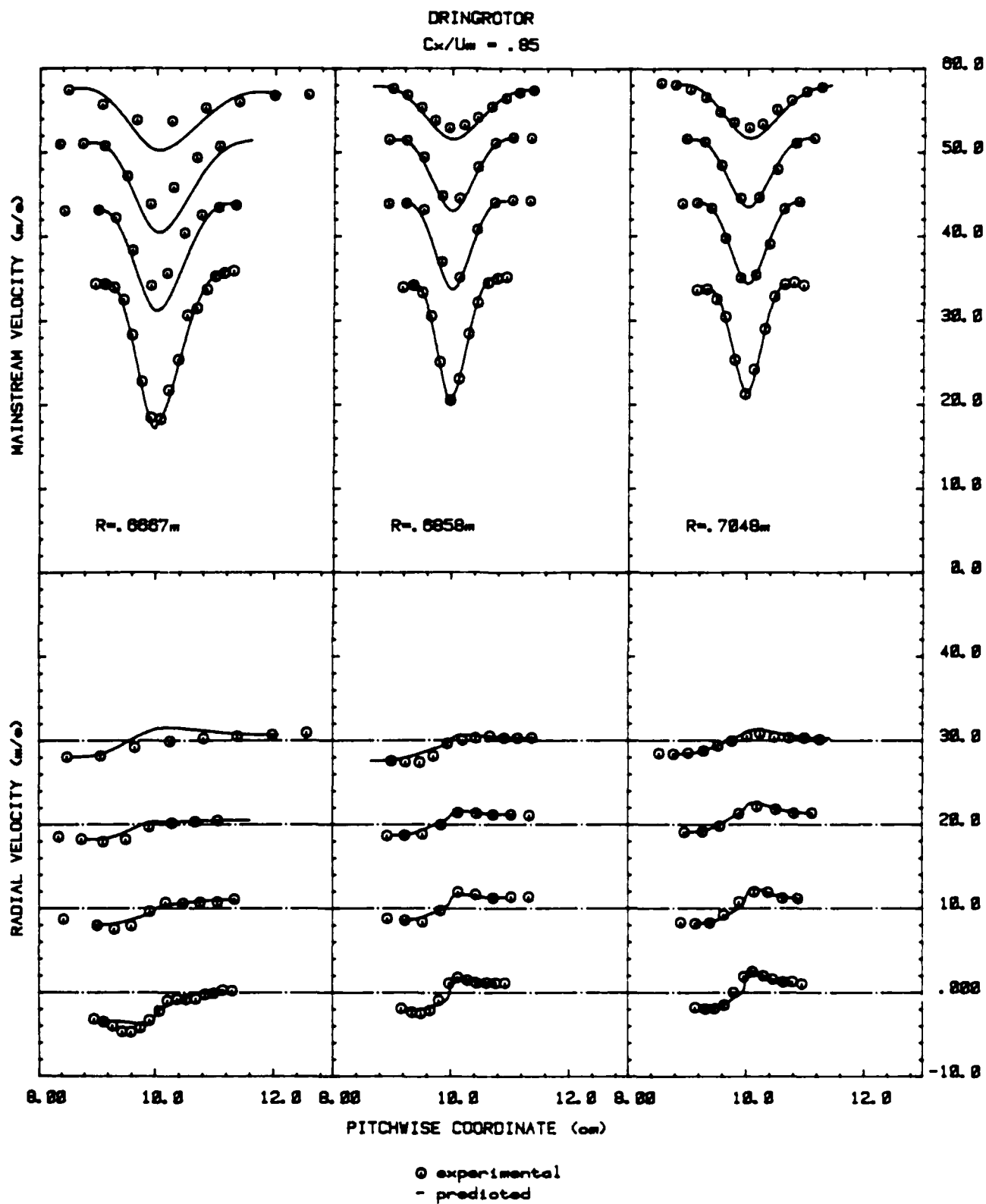


Figure 9.12

A.1 Some notions of curvature

In the present appendix some notions of curvature are reviewed and applied to the vector operations such as divergence and rotation.

It can be shown that in each orthogonal coordinate system, a set of coordinates x_1, x_2, x_3 with unit vectors e_1, e_2, e_3 can be defined in such a way that all the surfaces $x_1 = \text{cte}$, $x_2 = \text{cte}$, $x_3 = \text{cte}$ intersect in three orthogonal curves. x_1 , x_2 and x_3 , as well as their dimensions, are a priori unknown functions, except for special cases of orthogonal coordinates. In a cylindrical coordinate system for example, x_1, x_2, x_3 are found to be x, r, θ with as dimensions $L, L, 1$.

The length δl_i along the coordinate line δx_i is by definition given by

$$\delta l_i = h_i \delta x_i \quad (\text{A.1})$$

where h_1, h_2, h_3 are the lame or metric coefficients, which are also a priori unknown functions (e.g. the cylindrical coordinate system : $h_1 = h_2 = 1$, $h_3 = r$)

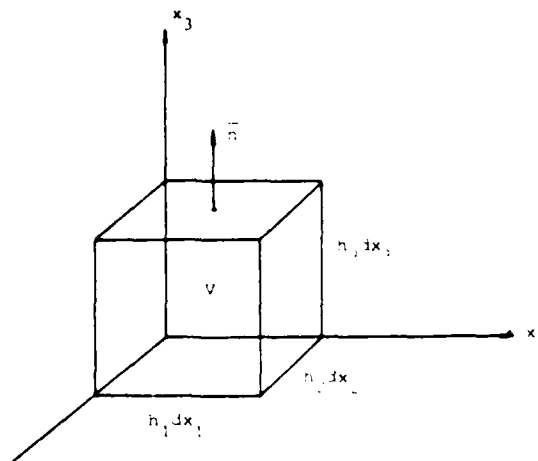


Figure A.1 : Elementary volume in curvilinear coordinates

The gradient operation can easily be expressed in a curvilinear coordinate system, since from

$$\frac{\partial \phi}{\partial n} = \vec{t}_n \cdot (\vec{\nabla} \phi) \quad (\text{A.2})$$

it easily follows that

$$\vec{\nabla}\phi = \left(\vec{e}_1 \frac{\partial}{\partial l_1} + \vec{e}_2 \frac{\partial}{\partial l_2} + \vec{e}_3 \frac{\partial}{\partial l_3} \right) \phi \quad (\text{A.3})$$

When applying the nabla operator to a vector or a tensor, derivatives of the unit vectors \vec{e}_i however appear which are non-zero due to curvature. Hence correction terms in general appear when applying equations of motion in curvilinear systems. In order to determine these corrections, the general definition of the nabla operator will be introduced [Milne] (fig A.1)

$$\vec{\nabla} \cdot X = \lim_{V \rightarrow 0} \frac{1}{V} \int_S \vec{n} \cdot X \, dS \quad (\text{A.4})$$

where X denotes as well a scalar as a vector or a tensor. Choosing an elementary volume dV with dimensions $h_i dx_i$, and applying eq A.4, it is easily found that

$$\vec{\nabla} \cdot \vec{V} = \frac{1}{h_1 h_2 h_3} \left[\frac{\partial}{\partial x_1} h_2 h_3 V_1 + \frac{\partial}{\partial x_2} h_1 h_3 V_2 + \frac{\partial}{\partial x_3} h_1 h_2 V_3 \right] \quad (\text{A.5})$$

$$\vec{\nabla} \cdot \vec{\tau} = \frac{1}{h_1 h_2 h_3} \left[\frac{\partial}{\partial x_1} h_2 h_3 \vec{\tau}_1 + \frac{\partial}{\partial x_2} h_1 h_3 \vec{\tau}_2 + \frac{\partial}{\partial x_3} h_1 h_2 \vec{\tau}_3 \right] \quad (\text{A.6})$$

From eq A.5 it follows that e.g. for \vec{e}_i

$$\vec{\nabla} \cdot \vec{e}_1 = \frac{1}{h_1 h_2 h_3} \frac{\partial}{\partial x_1} h_2 h_3 \quad (\text{A.7})$$

Hence, eqs A.5 and A.6 can be rewritten as (sum over i and j)

$$\vec{\nabla} \cdot \vec{V} = \frac{\partial V_i}{\partial l_i} + V_i (\vec{\nabla} \cdot \vec{e}_i) \quad (\text{A.8})$$

$$\vec{\nabla} \cdot \vec{\tau} = \vec{e}_j \frac{\partial \tau_{ij}}{\partial l_i} + \tau_{ij} \frac{\partial \vec{e}_j}{\partial l_i} + \vec{\tau}_i (\vec{\nabla} \cdot \vec{e}_i) \quad (\text{A.9})$$

$$\text{where } \vec{\tau}_i = \tau_{ij} \vec{e}_j$$

In eqs (A.8) and (A.9), the correction terms due to curvature appear as functions of derivatives of the unit vectors.

Since the length corresponding to δx_i is $h_i \delta x_i$, it can easily be seen

from fig A.2 that for example

$$\frac{1}{h_2} \frac{\partial \vec{e}_1}{\partial x_2} = - \frac{1}{R_{21}} \vec{e}_2 \quad (\text{A.10})$$

where R_{21} is the radius of curvature of the plane curve obtained by intersection of the surface $x_1 = \text{cte}$ with the plane $(\vec{e}_1, \delta \vec{e}_1)$, or (\vec{e}_1, \vec{e}_2) (fig A.2). According to the theorem of Meusnier, this radius of curvature can be related to R_2 , the principal radius of curvature of x_2 through (fig A.2)

$$R_{21} = \frac{R_2}{\cos \theta_{21}} \quad (\text{A.11})$$

θ_{21} is the angle between \vec{e}_1 and the principal normal of x_2 .

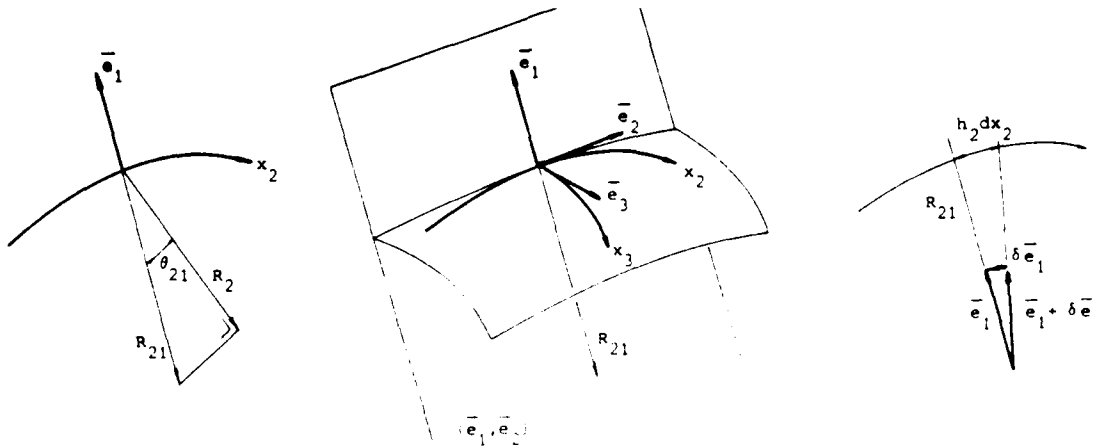


Figure A.2 : Radii of curvature in curvilinear coordinates

From eqs A.7 and A.10 repeated for each R_{ij} it can be shown that e.g. for \vec{e}_1

$$\frac{1}{h_1} \frac{\partial \vec{e}_1}{\partial x_1} = \frac{1}{R_{12}} \vec{e}_2 + \frac{1}{R_{13}} \vec{e}_3 \quad (\text{A.12})$$

$$\vec{\nabla} \vec{e}_1 = - \frac{1}{R_{21}} \vec{e}_2 - \frac{1}{R_{31}} \vec{e}_3 \quad (\text{A.13})$$

Hence, if all the radii R_{ij} are known functions, the correction terms in eqs A.8 and A.9 are known, while the functions x_i and h_i can -principally- be determined from

$$\frac{1}{R_{ij}} = - \frac{1}{h_i h_j} \frac{\partial h_i}{\partial x_j} \quad (\text{A.14})$$

A.2 The meridional coordinate system

The meridional coordinate system is illustrated on fig 3.1. In general curvature is present in both circumferential and meridional directions. The corresponding coordinates are m, n, u where m denotes the meridional direction, n the direction normal to the end-wall and u is the pitchwise direction. m, n and u are defined as lengths. The independent coordinates are denoted as x_m, x_n and x_u and the corresponding metric coefficients as h_m, h_n, h_u .

The direction u is taken positive in the direction normal to the profile walls, while n is always taken positive from the hub wall. Hence, if the pressure side coordinate system is right handed, the suction side coordinate system will be left handed, and vice-versa.

According to the theorem of Dupin, the system of coordinates m, n, u is an orthogonal coordinate system, since the m and u lines are lines of principal curvature. A rigorous development in non-orthogonal streamline coordinates is not considered.

The different radii of curvature of the coordinate lines along the blade profiles are found to be (fig 3.1)

$$\frac{1}{R_{mn}} = \frac{1}{R_m} = + \left. \frac{\partial \sigma}{\partial m} \right|_n \quad (\text{A.15})$$

$$\frac{1}{R_{mu}} = 0 \quad (\text{A.16})$$

$$\frac{1}{R_{nm}} = \frac{1}{R_n} = - \left. \frac{\partial \sigma}{\partial n} \right|_m \quad (\text{A.17})$$

$$\frac{1}{R_{nu}} = 0 \quad (\text{A.18})$$

$$\frac{1}{R_{um}} = - \frac{1}{r} \left. \frac{\partial r}{\partial m} \right|_n = - \frac{\sin \sigma}{r} \quad (\text{A.19})$$

$$\frac{1}{R_{un}} = - \frac{1}{r} \left. \frac{\partial r}{\partial n} \right|_m = - \frac{\cos \sigma}{r} \quad (\text{A.20})$$

According to section A.1, the knowledge of these radii allows the application of any vector operation in the meridional coordinate system.

From eqs (A.14), (A.19) and (A.20), it follows that

$$x_u = \theta \quad (A.21)$$

$$h_u = r \quad (A.22)$$

h_m , h_n , x_m and x_n cannot be determined explicitly for an arbitrary wall shape. Due to axisymmetry, it however follows from eqs (A.14), (A.16) and (A.18) that

$$\frac{\partial h_m}{\partial x_u} = \frac{\partial h_n}{\partial x_u} = 0 \quad (A.23)$$

It is to be observed that eqs (A.15) to (A.20) are valid in both pressure and suction side m,n,u coordinate systems which are respectively right and left handed or vice-versa. Care must be taken when choosing the sign convention of σ .

In the present appendix, the momentum equations are reconstructed taking wall curvature and variable inviscid flow parameters into account. In the following, the flow variables denoted with a carat $\hat{\cdot}$ are those obtained from the quasi 3D computations. The integral boundary layer approach seeks for the differences between these variables and the real flow variables.

Both flows must satisfy continuity, subtraction of both conditions yields (in the blade reference system)

$$\vec{\nabla} \cdot (\hat{\rho} \vec{\hat{W}} - \rho \vec{W}) = 0 \quad (B.1)$$

According to eq (A.5), eq (B.1) can be written as

$$\begin{aligned} & \frac{\partial}{\partial x_m} h_n h_u (\hat{\rho} \hat{w}_m - \rho w_m) \\ & + \frac{\partial}{\partial x_n} h_m h_u (\hat{\rho} \hat{w}_n - \rho w_n) \\ & + \frac{\partial}{\partial x_u} h_m h_n (\hat{\rho} \hat{w}_u - \rho w_u) = 0 \end{aligned} \quad (B.2)$$

Eq (B.2) will be integrated over the boundary layer. The integration of eq (B.2) yields

$$\begin{aligned} & \int_0^{x_{u\delta}} \frac{\partial}{\partial x_m} h_n h_u (\hat{\rho} \hat{w}_m - \rho w_m) dx_u + \int_0^{x_{u\delta}} \frac{\partial}{\partial x_n} h_m h_u (\hat{\rho} \hat{w}_n - \rho w_n) dx_u \\ & + [h_m h_n (\hat{\rho} \hat{w}_u - \rho w_u)]_0^{x_{u\delta}} = 0 \end{aligned} \quad (B.3)$$

where

$$\begin{aligned} w_u &= 0 \quad \text{at} \quad x_u = 0 \\ \hat{W} &= \vec{W} \quad \text{at} \quad x_u = x_{u\delta} \end{aligned} \quad (B.4)$$

Using eqs (A.1), (A.21) and (A.22), eq (B.3) can be rewritten as

$$\begin{aligned}
[h_m h_n \hat{\rho} \hat{w}_u]_w &= \frac{\partial}{\partial x_m} \int_0^\delta (\hat{\rho} \hat{w}_m - \rho w_m) h_n r d\theta \\
&+ \frac{\partial}{\partial x_n} \int_0^\delta (\hat{\rho} \hat{w}_n - \rho w_n) h_m r d\theta
\end{aligned}
\tag{B.5}$$

The subscript w stands for 'wall'. It is to be observed that the derivatives have been put outside of the integral sign in eq (B.5). This may be done since the function to be integrated becomes zero at $x_u(\delta)$.

The momentum equation 3.3 for variable inviscid flows is to be rewritten as

$$\hat{\rho}(\vec{\vec{W}}\vec{\vec{V}})\vec{\vec{W}} - \rho(\vec{\vec{W}}\vec{\vec{V}})\vec{\vec{W}} + 2\omega\Lambda(\hat{\rho}\vec{\vec{W}} - \rho\vec{\vec{W}}) = -\vec{\vec{p}}(\hat{p} - p) + \vec{\vec{p}}(\vec{\vec{\tau}} - \vec{\vec{\tau}})
\tag{B.6}$$

In eq B.6, the difference in momentum between the inviscid and the real flow is equated. Through the use of inviscid flow parameters as reference ones, radial equilibrium is taken into account inside the EWB. In the following the four contributions in eq B.6 will be analysed separately.

B.1 Inertial contribution

The mainstream projection of $(\vec{\vec{W}}\vec{\vec{V}})\vec{\vec{W}}$ is found to be

$$\vec{e}_m \cdot (\vec{\vec{W}}\vec{\vec{V}})\vec{\vec{W}} = \frac{w_m}{h_m} \frac{\partial w_m}{\partial x_m} + \frac{w_n}{h_n} \frac{\partial w_m}{\partial x_n} + \frac{w_u}{h_u} \frac{\partial w_m}{\partial x_u} + w_n \left(\frac{w_n}{R_{nm}} - \frac{w_m}{R_{mn}} \right) + w_u \left(\frac{w_u}{R_{um}} - \frac{w_m}{R_{mu}} \right)
\tag{B.7}$$

Hence, taking $h_m h_n h_u$ times eq B.7, the \vec{e}_m projection of the inertial contribution of eq B.6 can be rewritten as

$$\begin{aligned}
& h_m h_n h_u \vec{e}_m \cdot [\rho(\vec{w}\vec{v})\vec{w} - \rho(\vec{w}\vec{v})\vec{w}] = \\
& h_n h_u \left[\hat{\rho} \hat{w}_m \frac{\partial \hat{w}_m}{\partial x_m} - \rho w_m \frac{\partial w_m}{\partial x_m} \right] \\
& + h_m h_u \left[\hat{\rho} \hat{w}_n \frac{\partial \hat{w}_m}{\partial x_n} - \rho w_n \frac{\partial w_m}{\partial x_n} \right] \\
& + h_m h_n \left[\hat{\rho} \hat{w}_u \frac{\partial \hat{w}_m}{\partial x_u} - \rho w_u \frac{\partial w_m}{\partial x_u} \right] \quad (B.8) \\
& - \frac{h_m h_n h_u}{R_{mn}} \left[\hat{\rho} \hat{w}_m \hat{w}_n - \rho w_m w_n \right] \\
& + \frac{h_m h_n h_u}{R_{nm}} \left[\hat{\rho} \hat{w}_n^2 - \rho w_n^2 \right] \\
& + \frac{h_m h_n h_u}{R_{um}} \left[\hat{\rho} \hat{w}_u^2 - \rho w_u^2 \right]
\end{aligned}$$

$1/R_{mu}$ is zero due to axisymmetry. The last three terms in eq B.8 are correction terms due to wall curvature.

Integration of the third term in the lhs of eq B.8 with respect to x_u over the boundary layer yields

$$[h_m h_n (\hat{\rho} \hat{w}_m \hat{w}_u - \rho w_m w_u)]_0^{x_{u\delta}} - \int_0^{x_{u\delta}} (\hat{w}_m \frac{\partial}{\partial x_u} h_m h_n \hat{\rho} \hat{w}_u - w_m \frac{\partial}{\partial x_u} h_m h_n \rho w_u) dx_u \quad (B.9)$$

The first term of B.9 reduces to

$$- (h_m h_n \hat{\rho} \hat{w}_m \hat{w}_u)_{\text{wall}} \quad (B.10)$$

and, according to eq 5.14 to

$$\begin{aligned}
& - \int \hat{w}_{mw} \frac{\partial}{\partial x_m} (\hat{\rho} \hat{w}_m - \rho w_m) h_n h_u dx_u \\
& - \int \hat{w}_{mw} \frac{\partial}{\partial x_n} (\hat{\rho} \hat{w}_n - \rho w_n) h_m h_u dx_u \quad (B.11)
\end{aligned}$$

According to the continuity equation B.5, the second term of B.9 can be

written as

$$\begin{aligned} & \int (\hat{w}_m \frac{\partial}{\partial x_m} h_n h_u \hat{\rho w}_m - w_m \frac{\partial}{\partial x_m} h_n h_u \rho w_m) dx_u \\ & + \int (\hat{w}_m \frac{\partial}{\partial x_n} h_m h_n \hat{\rho w}_n - w_m \frac{\partial}{\partial x_n} h_m h_n \rho w_n) dx_n \end{aligned} \quad (B.12)$$

With eqs B.9, B.11 and B.12, and according to eqs A.1 and A.14, eq B.8 can easily be rearranged to

$$\begin{aligned} & \int_0^x u \delta h_m h_n h_u \vec{e}_m \cdot [\rho(\vec{w}\vec{v})\vec{w} - \rho(\vec{w}\vec{v})\vec{w}] dx_u = \\ & \frac{\partial}{\partial x_m} \int (\hat{w}_m - w_m) \rho w_m h_n r d\theta - \frac{\partial}{\partial x_m} \int (\hat{w}_{mw} - \hat{w}_m)(\hat{\rho w}_m - \rho w_m) h_n r d\theta \\ & + \frac{\partial}{\partial x_n} \int (\hat{w}_m - w_m) \rho w_n h_m r d\theta - \frac{\partial}{\partial x_n} \int (\hat{w}_{mw} - \hat{w}_m)(\hat{\rho w}_n - \rho w_n) h_m r d\theta \\ & + h_n \frac{\partial \hat{w}_{mw}}{\partial x_m} \int (\hat{\rho w}_m - \rho w_m) r d\theta + h_m \frac{\partial \hat{w}_{mw}}{\partial x_n} \int (\hat{\rho w}_n - \rho w_n) r d\theta \\ & - \frac{h_m h_n}{R_{mn}} \int (\hat{\rho w}_m \hat{w}_n - \rho w_m w_n) r d\theta + \frac{h_m h_n}{R_{nm}} \int (\hat{\rho w}_n^2 - \rho w_n^2) r d\theta \\ & + \frac{h_m h_n}{R_{um}} \int (\hat{\rho w}_u^2 - \rho w_u^2) r d\theta \end{aligned} \quad (B.13)$$

In a similar way, the spanwise projection of the inertial term is found to be

$$\begin{aligned}
& \frac{\partial}{\partial x_m} \int (\hat{w}_n - w_n) \rho w_m h_n r d\theta - \frac{\partial}{\partial x_m} \int (\hat{w}_{nw} - \hat{w}_n) (\hat{\rho w}_m - \rho w_m) h_n r d\theta \\
& + \frac{\partial}{\partial x_n} \int (\hat{w}_n - w_n) \rho w_n h_m r d\theta - \frac{\partial}{\partial x_n} \int (\hat{w}_{nw} - \hat{w}_n) (\hat{\rho w}_n - \rho w_n) h_m r d\theta \\
& + h_n \frac{\partial \hat{w}_{nw}}{\partial x_m} \int (\hat{\rho w}_m - \rho w_m) r d\theta + h_m \frac{\partial \hat{w}_{nw}}{\partial x_n} \int (\hat{\rho w}_n - \rho w_n) r d\theta \quad (B.14) \\
& - \frac{h_m h_n}{R_{nm}} \int (\hat{\rho w}_m \hat{w}_n - \rho w_m w_n) r d\theta + \frac{h_m h_n}{R_{mn}} \int (\hat{\rho w}_m^2 - \rho w_m^2) r d\theta \\
& + \frac{h_m h_n}{R_{un}} \int (\hat{\rho w}_u^2 - \rho w_u^2) r d\theta
\end{aligned}$$

B.2 Coriolis contribution

The second contribution in eq B.6 will now be integrated over the boundary layer. This contribution which represents the coriolis effect can be rewritten as

$$\begin{aligned}
2\omega \Lambda (\hat{\rho \vec{w}} - \rho \vec{w}) &= 2\omega \left[(\hat{\rho w}_m - \rho w_m) \vec{e}_x \Lambda \vec{e}_m \right. \\
& \quad (\hat{\rho w}_n - \rho w_n) \vec{e}_x \Lambda \vec{e}_n \\
& \quad \left. (\hat{\rho w}_u - \rho w_u) \vec{e}_x \Lambda \vec{e}_u \right] \quad (B.15)
\end{aligned}$$

where

$$\begin{aligned}
\vec{e}_x \Lambda \vec{e}_m &= \pm \sin \sigma \vec{e}_u = \mp \frac{r}{R_{um}} \vec{e}_u \\
\vec{e}_x \Lambda \vec{e}_n &= \pm \cos \sigma \vec{e}_u = \mp \frac{r}{R_{un}} \vec{e}_u \quad (B.16) \\
\vec{e}_x \Lambda \vec{e}_u &= \mp \vec{e}_y = \mp \sin \sigma \vec{e}_m \mp \cos \sigma \vec{e}_n = \pm \frac{r}{R_{um}} \vec{e}_m \pm \frac{r}{R_{un}} \vec{e}_n
\end{aligned}$$

Eq B.16 may be written in both pressure and suction side coordinate systems, the upper and lower signs correspond respectively to right and left handed coordinate systems. According to eqs B.15 and B.16, the m and n projections

of the coriolis term are found to be respectively

$$\pm 2\omega(\hat{\hat{\rho w}}_u - \rho w_u) \frac{r}{R_{um}} \quad (B.17)$$

$$\pm 2\omega(\hat{\hat{\rho w}}_u - \rho w_u) \frac{r}{R_{un}} \quad (B.18)$$

As for the first contribution of eq B.6, eqs B.17 and B.18 are multiplied by $h_m h_n h_u$ and next integrated with respect to dx_u over the boundary layer giving respectively

$$\pm 2\omega \frac{r}{R_{um}} h_m h_n \int (\hat{\hat{\rho w}}_u - \rho w_u) r d\theta \quad (B.19)$$

$$\pm 2\omega \frac{r}{R_{un}} h_m h_n \int (\hat{\hat{\rho w}}_u - \rho w_u) r d\theta \quad (B.20)$$

B.4 Shear stress contribution

The last contribution which is finally to be analysed is the shear stress contribution. According to eq A.6, this contribution can be written as (sum over j)

$$\begin{aligned} h_m h_n h_u \vec{\nabla} \vec{\tau} &= \frac{\partial}{\partial x_m} h_n h_u \tau_{mj} \vec{e}_j + \frac{\partial}{\partial x_n} h_m h_u \tau_{nj} \vec{e}_j + \frac{\partial}{\partial x_u} h_m h_n \tau_{uj} \vec{e}_j \\ &= \vec{e}_j \left[\frac{\partial}{\partial x_m} h_n h_u \tau_{mj} + \frac{\partial}{\partial x_n} h_m h_u \tau_{nj} + \frac{\partial}{\partial x_u} h_m h_n \tau_{uj} \right] \\ &\quad + h_n h_u \tau_{mj} \frac{\partial \vec{e}_j}{\partial x_m} + h_m h_u \tau_{nj} \frac{\partial \vec{e}_j}{\partial x_n} + h_m h_n \tau_{uj} \frac{\partial \vec{e}_j}{\partial x_u} \end{aligned} \quad (B.21)$$

The meridional projection of eq B.21 is found to be, according to A.10, A.12

$$\begin{aligned} h_m h_n h_u \vec{e}_m \cdot \vec{\nabla} \vec{\tau} &= \frac{\partial}{\partial x_m} h_n h_u \tau_{mm} + \frac{\partial}{\partial x_n} h_m h_u \tau_{nm} + \frac{\partial}{\partial x_u} h_m h_n \tau_{um} \\ &\quad + h_m h_n h_u \left[\frac{\tau_{nn}}{R_n} - \frac{\tau_{mn}}{R_m} + \frac{\tau_{uu}}{R_{um}} \right] \end{aligned} \quad (B.22)$$

Written as a defect and integrated over the boundary layer with respect to dx_u the mainstream contribution of the shear stress terms is easily found to

be

$$\begin{aligned}
 \int h_m h_n h_u \vec{e}_m \cdot \vec{\nabla} (\hat{\tau} - \tau) dx_u &= \int \frac{\partial}{\partial x_m} (\hat{\tau}_{mm} - \tau_{mm}) h_n r d\theta + \int \frac{\partial}{\partial x_n} (\hat{\tau}_{nm} - \tau_{nm}) h_n r d\theta \\
 &+ [h_m h_n (\hat{\tau}_{um} - \tau_{um})]_0^\delta \quad (B.23) \\
 &+ \int \left(\frac{\tau_{nn} - \tau_{nn}}{R_{nm}} - \frac{\tau_{mn} - \tau_{mn}}{R_{mn}} + \frac{\tau_{uu} - \tau_{uu}}{R_{um}} \right) h_m h_n r d\theta
 \end{aligned}$$

only the central term is hold, assuming the other terms of smaller order of magnitude. Assuming the shear stress tangential at the blade wall, the blade shear stress τ_s can be written as

$$\vec{\tau}_s = \vec{i}_m \cos \beta \tau_s + \vec{i}_u \sin \beta \tau_s \quad (B.24)$$

On the other hand, τ_s can be transformed from the other shear stresses through

$$\vec{\tau}_s = \vec{i}_s \cdot \vec{\tau} \quad (B.25)$$

$$\vec{\tau}_s = \vec{\tau}_u \cos \beta - \vec{\tau}_m \sin \beta = (\tau_{um} \vec{i}_m + \tau_{uu} \vec{i}_u) \cos \beta - (\tau_{mm} \vec{i}_m + \tau_{mu} \vec{i}_u) \sin \beta$$

Hence τ_s is found to be given by

$$\begin{aligned}
 \tau_s &= \tau_{um} - \tau_{mm} \tan \beta = -\tau_{mu} + \tau_{uu} / \tan \beta \quad (B.26) \\
 \tau_s &\approx \tau_{um}
 \end{aligned}$$

In this appendix integral boundary layer parameters are listed as functions of the boundary layer parameters δ , n , b and $\text{tg}\epsilon'_w$. The thickness δ is not an independent variable and it is shown how it can be eliminated. Basic thicknesses are expressed as direct functions of these parameters, and others are derived from the basic thicknesses. The different components of the Jacobian matrix are listed. All the equations are written in the meridional wall reference system.

The basic model equations which are used are remembered to be

$$\frac{w_s}{x} = 1 - b (1 - \eta)^n \quad (\text{C.1})$$

$$\frac{w_n - w_s \text{tg}\alpha}{w_s} = (1-b) \text{tg}\epsilon'_w (1 - \eta)^n \quad (\text{C.2})$$

with as complementary relations

$$b = \exp(-10n \sqrt{C_f}) \quad (\text{C.3})$$

$$C_f = .246 \text{Re}_{\theta'_{ss}}^{-.268} \frac{\hat{T}}{T^*} e^{-1.56H} \quad (\text{C.4})$$

The meridional thicknesses are defined through

$$\hat{\rho w}_{m\theta ij}^2 = \int_0^\delta (\hat{w}_i - w_i) \rho w_j r d\theta \quad (\text{C.5})$$

$$\hat{\rho w}_{m\delta i}^* = \int_0^\delta (\hat{\rho w}_i - \rho w_i) r d\theta \quad (\text{C.6})$$

The integrations in C.5 and C.6 are taken along u lines. Working along lines normal to the blade surface yields following expressions

$$\hat{\rho w}_{s\theta ij}^2 = \delta' \int_0^1 (\hat{w}_i - w_i) \rho w_j dn \quad (\text{C.7})$$

$$\hat{\rho w}_{s\delta i}^* = \delta' \int_0^1 (\hat{\rho w}_i - \rho w_i) dn \quad (\text{C.8})$$

According to eqs C.1 to C.8, it is easily shown that

$$\theta'_{ss} = \delta' b (f_1 - f_2) \quad (C.9)$$

$$\delta'_s = \delta' b f_1 \quad (C.10)$$

where

$$f_i = \frac{b^{i-1}}{in+1} \quad (C.11)$$

The other thicknesses are easily found to be

$$\delta'_n = \delta'_s (tg\alpha - \frac{1-b}{b} tg\epsilon'_w) \quad (C.12)$$

$$\theta'_{ns} = \theta'_{ss} (tg\alpha - \frac{1-b}{b} tg\epsilon'_w) \quad (C.13)$$

$$\theta'_{nn} = \theta'_{sn} (tg\alpha - \frac{1-b}{b} tg\epsilon'_w) \quad (C.14)$$

$$\theta'_{sn} = \theta'_{ss} (tg\alpha - \frac{1-b}{b} tg\epsilon'_w) + \delta'_s \frac{1-b}{b} tg\epsilon'_w \quad (C.15)$$

$$\theta'_{nn} = \theta'_{ns} (tg\alpha - \frac{1-b}{b} tg\epsilon'_w) + \delta'_n \frac{1-b}{b} tg\epsilon'_w \quad (C.16)$$

The relation between the two sets of thicknesses is found from

$$\begin{aligned} rd\theta &= \delta' dn / \cos\beta \\ w_m &= w_s \cos\beta \\ w_u &= w_s \sin\beta \end{aligned} \quad (C.17)$$

Application of C.17 in the different definitions yields

$$\delta = \delta' / \cos \beta$$

$$w_{m\ mm}^2 \theta = w_m w_s \theta'_{ss}$$

$$w_{m\ nm}^2 \theta = w_s^2 \theta'_{ns}$$

$$w_{m\ mn}^2 \theta = w_s^2 \theta'_{sn} \quad (C.18)$$

$$w_{m\ nn}^2 \theta = w_s^2 \theta'_{nn} / \cos \beta$$

$$w_m \delta_m^* = w_s \delta_s^*$$

$$w_m \delta_n^* = w_s \delta_n^* / \cos \beta$$

Using eqs C.9 to C.18 all the classical thicknesses can be determined from the knowledge of n , b and ϵ'_w . The shape factio H is to found from

$$H = \frac{1}{1 - b \frac{n+1}{2n+1}} \quad (C.19)$$

The independent variables which are used in the method are defined as follows

$$\{q\} = \{ \ln(-\ln b) , \ln(n) , \text{tg} \epsilon'_w \} \quad (C.20)$$

The corresponding components of the jacobian matrix J between the thicknesses and the parameters q are obtained as follows. Differentiation of eq C.4 yields

$$\frac{d(\rho w_{m\ mm}^2 \theta)}{\rho w_{m\ mm}^2 \theta} = \frac{d(\rho w_m w_s \theta'_{ss})}{\rho w_m w_s \theta'_{ss}} = - 3.73 \frac{dC_f}{C_f} - 5.82 dH + \frac{d\rho w_m}{\rho w_m} \quad (C.21)$$

where, according to eqs C.3

$$\frac{dC_f}{C_f} = 2 d[\ln(-\ln b)] - 2 d[\ln(n)] \quad (C.22)$$

which explains the choice of q in eq C.20. dH is given by

$$\begin{aligned} dH &= H^2 \frac{2n+1}{n+1} \left(\frac{db}{b} - \left(\frac{2}{2n+1} - \frac{1}{n+1} \right) dn \right) \\ &= H^2 \frac{f_2}{f_1} \left(\ln b \cdot d[\ln(-\ln b)] - \left(\frac{2}{2n+1} - \frac{1}{n+1} \right) n \cdot d[\ln(n)] \right) \end{aligned} \quad (C.23)$$

Hence, the derivatives of $\rho w_m^2 \theta_{mm}$ are found to be

$$\frac{\partial}{\partial q_1} \rho w_m^2 \theta_{mm} = - \rho w_m^2 \theta_{mm} \left[7.4627 + 5.82 H_k^2 \frac{f_2}{f_1} \ln b \right] \quad (C.24)$$

$$\frac{\partial}{\partial q_2} \rho w_m^2 \theta_{mm} = \rho w_m^2 \theta_{mm} \left[7.4627 + 5.82 H_k^2 \frac{f_2}{f_1} \left(\frac{2}{2n+1} - \frac{1}{n+1} \right) n \right] \quad (C.25)$$

$$\frac{\partial}{\partial q_3} \rho w_m^2 \theta_{mm} = 0 \quad (C.26)$$

$$\frac{\partial}{\partial m} \rho w_m^2 \theta_{mm} = \rho w_m^2 \theta_{mm} \frac{1}{\rho w_m} \frac{\partial \rho w_m}{\partial m} \quad (C.27)$$

The derivatives of $\rho w_m^2 \theta_{nm}$ are found from eq C.18 and C.23.

$$\begin{aligned} \rho w_m^2 \theta_{nm} &= \rho w_s^2 \theta'_{ns} \\ &= \rho w_s^2 \theta'_{ss} \left(\frac{\theta'_{ns}}{\theta'_{ss}} \right) \\ &= \rho w_m^2 \theta_{mm} \frac{w_s}{w_m} \left(\operatorname{tg} \alpha - \frac{1-b}{b} \operatorname{tg} \epsilon'_w \right) \end{aligned} \quad (C.28)$$

derivation of, in logarithmic form yields

$$\begin{aligned} \frac{d(\rho w_m^2 \theta_{nm})}{\rho w_m^2 \theta_{nm}} &= \frac{d(\rho w_m^2 \theta_{mm})}{\rho w_m^2 \theta_{mm}} + \frac{w_s \theta_{mm}}{w_m \theta_{nm}} d \left(\operatorname{tg} \alpha - \frac{1-b}{b} \operatorname{tg} \epsilon'_w \right) \\ &\quad + \cos \beta d \left(\frac{1}{\cos \beta} \right) \end{aligned} \quad (C.29)$$

$$\frac{\partial}{\partial q_1} \rho w_m^2 \theta_{nm} = \frac{\theta_{nm}}{\theta_{mm}} \frac{\partial}{\partial q_1} \rho w_m^2 \theta_{mm} + \rho w_s w_m \theta_{mm} \operatorname{tg} \epsilon'_w \frac{\ln b}{b} \quad (C.30)$$

$$\frac{\partial}{\partial q_2} \rho w_m^2 \theta_{nm} = \frac{\theta_{nm}}{\theta_{mm}} \frac{\partial}{\partial q_2} \rho w_m^2 \theta_{mm} \quad (C.31)$$

$$\frac{\partial}{\partial q_3} \rho w_m^2 \theta_{nm} = - \frac{1-b}{b} \rho w_m w_s \theta_{mm} \quad (C.32)$$

$$\frac{\partial}{\partial m} \rho w_m^2 \theta_{nm} = \frac{\theta_{nm}}{\theta_{mm}} \frac{\partial}{\partial m} \rho w_m^2 \theta_{mm} + \rho w_m w_s \left(\theta_{mm} \frac{\partial}{\partial m} \operatorname{tg} \alpha - \theta_{nm} \frac{\partial}{\partial m} \cos \beta \right) \quad (C.33)$$

The derivatives of $\delta-\delta_m^*$ finally follow from the definition of H^*

$$\frac{d(\rho w_m (\delta-\delta_m^*))}{\rho w_m (\delta-\delta_m^*)} = \frac{d(\rho w_m^2 \theta_{mm})}{\rho w_m^2 \theta_{mm}} + \frac{dH^*}{H^*} - \frac{dw_m}{w_m} \quad (C.34)$$

Differentiation yields

$$\frac{\partial}{\partial q_1} \rho w_m (\delta-\delta_m^*) = \rho w_m (\delta-\delta_m^*) \left(\frac{1}{\rho w_m^2 \theta_{mm}} \frac{\partial}{\partial q_1} \rho w_m^2 \theta_{mm} + b \ln b \frac{1}{H^*} \frac{\partial H^*}{\partial b} \right) \quad (C.35)$$

$$\frac{\partial}{\partial q_2} \rho w_m (\delta-\delta_m^*) = \rho w_m (\delta-\delta_m^*) \left(\frac{1}{\rho w_m^2 \theta_{mm}} \frac{\partial}{\partial q_2} \rho w_m^2 \theta_{mm} + n \frac{1}{H^*} \frac{\partial H^*}{\partial n} \right) \quad (C.36)$$

$$\frac{\partial}{\partial q_3} \rho w_m (\delta-\delta_m^*) = 0 \quad (C.37)$$

$$\frac{\partial}{\partial m} \rho w_m (\delta-\delta_m^*) = \rho w_m (\delta-\delta_m^*) \frac{1}{\rho} \frac{\partial \rho}{\partial m} \quad (C.38)$$

The derivatives of H^* are found to be

$$\frac{1}{H^*} \frac{\partial H^*}{\partial b} = - \frac{f_1}{1 - b f_1} - \frac{f_1 - 2f_2}{b(f_1 - f_2)} \quad (C.39)$$

$$\frac{1}{H^*} \frac{\partial H^*}{\partial n} = - \frac{\frac{\partial}{\partial n} f_1}{1 - b f_1} - \frac{\frac{\partial}{\partial n} f_1 - \frac{\partial}{\partial n} f_2}{f_1 - f_2} \quad (C.40)$$

APPENDIX D : INTEGRAL WAKE PARAMETERS

In this appendix integral wake parameters are listed as functions of the wake parameters δ , b and $\text{tg}\epsilon'_w$. Basic thicknesses are expressed as direct functions of these parameters, and others are derived from the basic thicknesses. The different components of the Jacobian matrix are listed. All the equations are written in the meridional blade reference system.

The basic model equations which are used are

$$\frac{w_s^+}{w_s} = 1 - b^+ f(\eta) - (\bar{b} - b^+) g(\eta) \quad (\text{D.1})$$

$$\frac{w_n^+ - w_s^+ \text{tg}\alpha^+}{w_s} = (1 - b^+) \text{tg}\epsilon^+ f(\eta) + ((1 - \bar{b})(\text{tg}\bar{\epsilon} + \text{tg}\bar{\alpha} - \text{tg}\alpha^+) - (1 - b^+) \text{tg}\epsilon^+) g(\eta) \quad (\text{D.2})$$

where

$$f(\eta) = 1 - 6\eta^2 + 8\eta^3 - 3\eta^4 \quad (\text{D.3})$$

$$g(\eta) = e^{-\eta/\eta_0} \quad (\text{D.4})$$

$$\eta_0 = \frac{1}{\delta} \sqrt{v \Delta m / w_m} \quad (\text{D.5})$$

where η_0 should not exceed about .5. Thicknesses in streamline coordinates are defined through

$$\hat{\hat{\rho w_s^2}}_{ij} = \delta' \int_0^1 (\hat{w}_i - w_i) \rho w_j d\eta \quad (\text{D.6})$$

$$\hat{\hat{\rho w_s}}_{i1}^* = \delta' \int_0^1 (\hat{\hat{\rho w_i}} - \rho w_i) d\eta \quad (\text{D.7})$$

According to eqs D.1 to D.7, it is easily shown that

$$\delta_s'^* = I_f + I_g \quad (\text{D.8})$$

$$\theta_{ss}' = \delta_s'^* - I_{ff} - I_{gg} - 2 I_{fg} \quad (\text{D.9})$$

$$\delta_n'^* = \delta_s'^* \operatorname{tg} \alpha - I_f^f - I_g^g \quad (\text{D.10})$$

$$\theta_{sn}' = \theta_{ss}' \operatorname{tg} \alpha + I_f^f + I_f^g + I_g^f + I_g^g \quad (\text{D.11})$$

$$\theta_{ns}' = \theta_{sn}' + \delta_n'^* - \delta_s'^* \operatorname{tg} \alpha \quad (\text{D.12})$$

$$\theta_{nn}' = (\theta_{sn}' + \theta_{ns}' - \theta_{ss}' \operatorname{tg} \alpha) \operatorname{tg} \alpha - I^{ff} - I^{gg} - 2I^{fg} \quad (\text{D.13})$$

where

$$I_f^g = \delta \xi_f \xi_g \int f g \, d\eta \quad (\text{D.14})$$

$$\frac{w_s}{x_s} = 1 - \xi_f f(\eta) - \xi_g g(\eta) \quad (\text{D.15})$$

$$\frac{w_n - w_s \operatorname{tg} \alpha}{x_s} = \xi_f^f f(\eta) + \xi_g^g g(\eta) \quad (\text{D.16})$$

$$\xi_f = b$$

$$\xi_g = \bar{b} - b \quad (\text{D.17})$$

$$\xi_f^f = (1-b) \operatorname{tg} \varepsilon$$

$$\xi_g^g = (1-\bar{b}) (\operatorname{tg} \bar{\varepsilon} + \operatorname{tg} \bar{\alpha} - \operatorname{tg} \alpha) - (1-b) \operatorname{tg} \alpha$$

using eqs D.3 and D.4 for f and g yields

$$\int f \, d\eta = \frac{2}{5}$$

$$\int f^2 \, d\eta = \frac{2}{7}$$

$$\int g \, d\eta = \eta_0 \quad (\text{D.18})$$

$$\int g^2 \, d\eta = \frac{\eta_0}{2}$$

$$\int f g \, d\eta = \eta_0 - 12\eta_0^3 + 48\eta_0^4 - 72\eta_0^5$$

The meridional thicknesses are found from (see appendix C)

$$rd\theta = \delta' dn / \cos\beta$$

$$w_m = w_s \cos\beta$$

(D.19)

$$w_u = w_s \sin\beta$$

Application of D.19 in the different definitions yields

$$\delta = \delta' / \cos\beta$$

$$w_{m\theta}^2 = w_m w_s \theta'$$

$$w_{m\theta}^2 = w_s^2 \theta'$$

$$w_{m\theta}^2 = w_s^2 \theta'$$

(D.20)

$$w_{m\theta}^2 = w_s^2 \theta' / \cos\beta$$

$$w_{m\delta}^* = w_s \delta'^*$$

$$w_{m\delta}^* = w_s \delta'^* / \cos\beta$$

END

FILMED

MARCH, 19 88

DTIC